

# A Businger Mechanism for Intermittent Bursting in the Stable Boundary

## Layer

Steven J. A. van der Linden\*

*Geoscience and Remote Sensing, Delft University of Technology, Delft, The Netherlands*

Bas J. H. van de Wiel

*Geoscience and Remote Sensing, Delft University of Technology, Delft, The Netherlands*

Igor Petenko

*Institute of Atmospheric Sciences and Climate, National Research Council, Rome, Italy and A. M.*

*Obukhov Institute of Atmospheric Physics, Russian Academy of Sciences, Moscow, Russia*

Chiel C. van Heerwaarden

*Meteorology and Air Quality Group, Wageningen University and Research, Wageningen, The*

*Netherlands*

Peter Baas, Harmen J. J. Jonker

*Geoscience and Remote Sensing, Delft University of Technology, Delft, The Netherlands*

\*Corresponding author address: S. J. A. van der Linden, Geoscience and Remote Sensing, Delft

University of Technology, Stevinweg 1, 2628 CN Delft, The Netherlands.

E-mail: [s.j.a.vanderlinden@tudelft.nl](mailto:s.j.a.vanderlinden@tudelft.nl)

**Early Online Release:** This preliminary version has been accepted for publication in *Journal of the Atmospheric Sciences*, may be fully cited, and has been assigned DOI 10.1175/JAS-D-19-0309.1. The final typeset copyedited article will replace the EOR at the above DOI when it is published.

## ABSTRACT

18 High-resolution large-eddy simulations of the Antarctic very stable bound-  
19 ary layer reveal a mechanism for systematic and periodic intermittent bursting.  
20 A non-bursting state with a boundary-layer height of just 3 m is alternated by  
21 a bursting state with a height of  $\approx 5$  m. The bursts result from unstable wave  
22 growth triggered by a shear-generated Kelvin–Helmholtz instability, as con-  
23 firmed by linear stability analysis. The shear at the top of the boundary layer  
24 is built up by two processes. The upper, quasi-laminar layer accelerates due  
25 to the combined effect of the pressure force and rotation by the Coriolis force,  
26 while the lower layer decelerates by turbulent friction. During the burst, this  
27 shear is eroded and the initial cause of the instability is removed. Subse-  
28 quently, the interfacial shear builds up again, causing the entire sequence to  
29 repeat itself with a timescale of  $\approx 10$  min. Despite the clear intermittent burst-  
30 ing, the overall change of the mean wind profile is remarkably small during the  
31 cycle. This enables such a fast erosion and recovery of the shear. This mecha-  
32 nism for cyclic bursting is remarkably similar to the mechanism hypothesized  
33 by Businger in 1973, with one key difference. Whereas Businger proposes  
34 that the flow acceleration in the upper layer results from downward turbu-  
35 lent transfer of high-momentum flow, the current results indicate no turbulent  
36 activity in the upper layer, hence requiring another source of momentum. Fi-  
37 nally, it would be interesting to construct a climatology of shear-generated  
38 intermittency in relation to large-scale conditions to assess the generality of  
39 this Businger mechanism.

## 40 1. Introduction

41 This study presents a mechanism for shear-generated intermittent turbulence in the very stable  
42 boundary layer (VSBL) based on a high-resolution large-eddy simulation (LES) study, which is  
43 representative for conditions on the Antarctic plateau (van der Linden et al. 2019). Here, with  
44 intermittent turbulence, we refer to “global intermittency” as defined by Mahrt (1999), where  
45 periods of ‘quiescent’ flow are interrupted by sudden bursts of turbulence. It is shown that shear is  
46 built up and eroded in a natural, cyclic manner at the top of the boundary layer. The high-shear flow  
47 then generates unstable waves that lead to turbulent bursting, which in turn erode the shear itself  
48 by which they are generated. Subsequently, a relatively ‘quiescent’ period follows during which  
49 shear is built up again. In this study, we will show that this shear-generated intermittency on short  
50 timescales ( $\approx 10$  min) is a systematic and periodic feature in our VSBL, and how it contributes to  
51 the steady-state VSBL over longer timescales ( $> 1$  h).

52 Shear-generated intermittent bursting is a frequently observed phenomenon within the weak-  
53 wind, stable boundary layer (SBL) (see, e.g., Nappo 1991; Mahrt 1999). In spite of its omnipres-  
54 ence, the reasons behind such intermittent flow have remained unclear as no general dominating  
55 mechanism has been identified (Mahrt 1999). Analyzing intermittent flow (from observations)  
56 is difficult because the turbulent intensity within the background flow is extremely weak. As  
57 such, the effects of local heterogeneities or case-specific disturbances are amplified, and the cause  
58 or origin of the burst is easily obscured. Multiple triggers of these events have been identified  
59 in literature, for example, density currents and solitary waves (Sun et al. 2004, 2012), spatially  
60 dependent (de)coupling depending on local topography (Acevedo and Fitzjarrald 2003), or the  
61 interplay between radiative surface cooling and pressure-gradient induced mixing (van de Wiel  
62 et al. 2002). Other frequently observed causes are unstable internal gravity waves resulting from

63 the Kelvin–Helmholtz instability (see, e.g., Gossard et al. 1970; Finnigan et al. 1984; de Baas and  
64 Driedonks 1985; Coulter 1990; Nappo 1991; Blumen et al. 2001).

65 Recently, Petenko et al. (2019) showed that successive wave disturbances frequently occur over  
66 periods exceeding several hours during the polar winter of 2012 at Dome C, Antarctica. It therefore  
67 appears to be a systematic feature of the long-lived Antarctic SBL. Using high-resolution sodar  
68 echogram observations, they were able to observe the fine-scale structure of such wave events and  
69 estimate both their characteristic temporal and spatial scales. In particular, they show that shear-  
70 generated wave disturbances occur under stationary conditions in periodic wave trains lasting 4–  
71 6 min even at supercritical bulk Richardson numbers ( $Ri_b > 0.25$ ).

72 Nearly half a century ago, Joost Businger proposed a mechanism by which such shear-generated  
73 bursts could occur in the VSBL even at supercritical Richardson numbers (see Businger 1973). He  
74 conjectured that, if the supercritical Richardson number is reached at a particular height, vertical  
75 transfer of momentum and heat is blocked. Locally, shear at this height builds up as the wind  
76 below is decelerated (vertical momentum flux divergence) and wind above is accelerated (con-  
77 vergence). The shear between the upper layer and lower layer increases until the flow becomes  
78 hydrodynamically unstable, and a burst of momentum and heat toward the surface can occur. The  
79 shear is rapidly reduced and the flow becomes quiescent again until the next burst. We will show  
80 that Businger’s mechanism is largely applicable except for one component. Whereas the lower  
81 layer is, indeed, decelerated by momentum divergence, momentum convergence is not the major  
82 cause of flow acceleration in the upper layer (as turbulent activity is very weak). Instead, the ac-  
83 celeration above is caused by the combination of the pressure force and wind turning due to the  
84 Coriolis force rather than by the assumed momentum convergence.

85 The favorable conditions in the Antarctic winter at the Dome C site may prove to be key in iden-  
86 tifying the mechanism for shear-generated intermittent bursts and its periodic occurrence. During

87 these Antarctic winter months (June to August), the SBL at Dome C may reach long periods  
88 (lasting for several days) of ‘steady state’ during which the wind and temperature profiles do not  
89 change significantly over time (Vignon et al. 2017b; Baas et al. 2019). The potential of the arctic  
90 regions has already been recognized before (see, e.g., Dabberdt 1970; Grachev et al. 2005, 2008)  
91 as they may serve as ‘natural laboratories’ for the study of the SBL—in particular—during the  
92 winter months when the daily cycle is absent.

93 By analysis of observations in combination with high-resolution LES, Van der Linden et al.  
94 (2019) show that, in the Antarctic, a thermal steady state is possible when the turbulent cooling of  
95 the SBL as a whole is balanced by heating through large-scale subsidence (see also Vignon et al.  
96 2018; Baas et al. 2019). The close correspondence between their LES results and the observations  
97 encourages the use of LESs for in-depth process studies. In contrast to the observations, within  
98 LESs, the boundary conditions and forcings can be fully controlled. Therefore, the LES approach  
99 is an attractive complementary tool to study the Antarctic SBL and the associated intermittency  
100 found by Petenko et al. (2019). However, they can only be considered complementary as simula-  
101 tions remain heavily idealized compared to complex reality with respect to, e.g., their forcing and  
102 surface boundary conditions (Bosveld et al. 2014). Such simulations have also been used before  
103 to study shear-generated instabilities in realistic settings, for example, based on CASES-99 (Zhou  
104 and Chow 2014) and the Beaufort Sea Arctic Stratus Experiments (Na et al. 2014).

105 Ideally, a full mechanistic analysis of intermittency directly from observations would be pre-  
106 ferred. Unfortunately, measuring such bursts is complicated by the harsh, cold conditions that  
107 make accurate measurements of turbulent fluxes by standard sonic-anemometers challenging (Vi-  
108 gnion et al. 2017a). Also, the sodar echogram data, although measured at relatively high spatiotem-  
109 poral resolution, are not easily transformed into quantitative fluxes (Petenko et al. 2019).

110 Somewhat surprisingly, the aforementioned LES results of van der Linden et al. (2019) indeed  
111 show the presence of periodic turbulent bursts in the VSBL similar to those reported by Petenko  
112 et al. (2019). Although the SBL is found to be in steady state with respect to its bulk quantities  
113 on an hourly basis, closer inspection reveals that the SBL is found to be periodically modulated  
114 by episodes of enhanced turbulence originating at the top of the boundary layer on timescales of  
115  $\approx 10$  min. These events subsequently spread both upward and downward resulting in a temporarily  
116 larger boundary-layer height and surface fluxes, respectively.

117 Here, we further investigate these top-down bursting events in the VSBL case of van der Linden  
118 et al. (2019) and show that they are the result of wave breaking after initial growth of a shear-  
119 generated instability. Using an extended simulation (viz., with a larger domain) at a high resolution  
120 ( $\Delta = 0.08$  m), the dominant wavelength is identified. The instability of this wave is confirmed by  
121 applying a linear stability analysis (LSA) on the background flow. Finally, we will identify the  
122 full intermittency cycle: the mechanism of wave growth, bursting, and erosion of the shear layer  
123 as well as the restoring mechanism to restore local shear again.

## 124 **2. The Steady Antarctic Boundary Layer?**

125 In this section, we further investigate the LES case of the VSBL of van der Linden et al. (2019)  
126 to show the presence of intermittent turbulence. A short overview of their VSBL simulation can  
127 be found in Appendix A. A comprehensive description of the observations and model formulation  
128 may be found in van der Linden et al. (2019).

129 Figure 1 shows the vertical profiles of the wind speed, potential temperature, kinematic temper-  
130 ature flux and the contributions to rate-of-change of potential temperature averaged over the final  
131 hour and the horizontal plane of the simulation. Van der Linden et al. (2019) show that on average  
132 (viz., averaged over simulation periods  $\geq 1$  h), a thermal steady state exists in which cooling of the

133 boundary layer by vertical divergence of the kinematic temperature flux is balanced by subsidence  
134 heating of the air. The heating rate of subsidence has a maximum at approximately 3.75 m, and  
135 decreases to zero toward the surface and top of the domain where the imposed subsidence velocity  
136 and temperature gradient are zero, respectively. Apparently, the profile of the temperature flux  
137 ‘adapts’ itself to the profile of subsidence heating, as the latter is a slower process (viz., the av-  
138 erage temperature gradient changes over timescales longer than the typical timescale of turbulent  
139 mixing).

140 Although the LES case is found to reach a thermal steady state averaged over periods  $\geq 1$  h,  
141 closer inspection indicates a thermal steady state does not exist over averaging periods of approxi-  
142 mately 10 minutes or shorter. Figure 2a presents the horizontally-averaged kinematic temperature  
143 flux as function of time and height during the final simulation hour of the original LES case. The  
144 temperature flux exhibits clear periodic behavior in which events of enhanced temperature flux are  
145 superimposed on a relatively ‘quiescent’ base state (i.e., a shallow SBL of depth  $z \approx 2.5\text{--}2.9$  m).  
146 These main bursting events appear to consistently start at the top of the boundary layer, and sub-  
147 sequently extent both upward and downward. After approximately 200s, the enhancement of the  
148 temperature flux has largely disappeared, although some enhanced values are still observed near  
149 the surface  $< 2$  m. The time between the onset of these successive events is approximately 600s.  
150 Similar patterns are also present in, for example, the horizontally-averaged momentum fluxes  
151 and temperature variance. Conceptually, a ‘short’ timescale of  $\approx 200$ s (or ‘fast’ process) can be  
152 defined in which the bursts affects the mean flow, and a ‘long’ timescale of  $\approx 400$ s (or ‘slow’  
153 process) in which the conditions favorable for the subsequent burst are created. As the magnitude  
154 of the bursts is relatively small (e.g.,  $O(10)$   $\text{W m}^{-2}$  in the heat flux), changes in the first-order  
155 statistics such as wind speed and temperature remain modest as well during an event; the standard  
156 deviations over the entire simulation hour are  $\sigma(U) < 0.04 \text{ m s}^{-1}$  and  $\sigma(\theta) = 0.29 \text{ K}$  (not shown).

157 Figure 2b shows the temporal relation of the kinematic temperature flux at the surface (green)  
158 and at the top of the SBL (i.e., at a height of 2.72 m; purple). During a burst, the 2.72-m flux  
159 rapidly exceeds the magnitude of the surface flux. On the contrary, the variation in the surface  
160 temperature flux is  $< 6\%$ , which indicates that bursts barely reach the surface. For convenience,  
161 we will define two states according to these two fluxes. The bursting intervals are defined as the  
162 periods in which the magnitude of temperature flux at 2.72 m exceeds the value of the surface flux.  
163 These intervals are indicated by the dash-dotted lines in Fig. 2b.

164 The observed behavior of the temperature flux is consistent with the formation and breaking  
165 of travelling waves at the interface of the turbulent boundary layer and the air aloft, which is  
166 confirmed by vertical cross sections from the simulation (see section 3a). During the initial stages  
167 of the bursting event, (linear) wave perturbations form and grow in time until nonlinear effects  
168 become dominant and cause wave breaking. Subsequently, turbulent kinetic energy is generated  
169 at this interface, which causes the boundary layer to grow in height (see Fig. 2a). Relatively warm  
170 and fast air is entrained into the boundary layer resulting in a net transport of both energy and  
171 momentum toward the surface (cf. Fig. 2b). This resembles the “upside-down” boundary layer as  
172 observed during the CASES-99 experiment (Mahrt and Vickers 2002).

173 In addition to these main events (at  $z \approx 2.5\text{--}2.9\text{ m}$ ), a secondary event appears to be initiated  
174 above the turbulent SBL in response to the first events (see  $z \approx 4.5\text{ m}$ ,  $t \approx 2800\text{ s}$ ). This secondary  
175 event is weak compared to the main events and appears not to penetrate deep into the base state.  
176 Its peak values are about 20% of those of the main events. Such secondary events appear to occur  
177 sporadically in the simulation. It is unclear if they result from a separate instability or from residual  
178 turbulence of the main bursting events. The turbulence on average is weak or even absent at higher  
179 levels in the flow ( $z > 4\text{ m}$ ), and the flow can be regarded as ‘quasi-laminar’ and decoupled from  
180 the surface layer (compare with Banta et al. 2007). Therefore, residual turbulence ejected by the

181 main events may take relatively long to dissipate. Due to its sporadic occurrence and weak impact,  
182 these secondary events are discarded in the main analysis.

### 183 3. Wave analysis

184 In this section, an in-depth analysis of the wave phenomenon is made. First, wave characteristics  
185 are diagnosed from the simulations. The dominant wavelength is extracted by spectral analysis of  
186 the vertical cross sections of the velocity field (see section 3a). Second, a linear stability analysis  
187 is applied in section 3b to show that the background flow is indeed unstable in time with respect  
188 to this wave perturbation, and that the wave growth enables turbulent bursting.

#### 189 a. Spectral analysis

190 To identify wave properties, such as, the wavelength or amplitude, vertical cross sections of the  
191 simulation are analyzed. Before applying the Fourier transform to find the dominant wavelength  
192 from the horizontal velocity fields, first a simple visual inspection is made. These suggest a wave-  
193 length of approximately 16–19 m in the original VSBL simulation of van der Linden et al. (2019)  
194 (not shown). Unfortunately, the full horizontal extent of the domain in their simulations amounts  
195 to only  $L_x = 19.2$  m (with an isotropic grid spacing of  $\Delta = 0.08$  m). Therefore, the wavenumber  
196 bin resolution (i.e., its detectable change)  $\Delta k$  is equal to  $0.3272 \text{ m}^{-1}$ , and accurate determination  
197 of the expected wavelength using spectral analysis is unfeasible.

198 To alleviate this problem, the original simulation is extended in both the horizontal directions  
199 according to the following procedure. First, five copies of the original simulation field at  $t = 23$  h  
200 are pasted together in the  $x$ -direction. Second, this ‘new’ field is duplicated and joined in the  $y$ -  
201 direction. Gaussian noise ( $\mu_G = 0$ ;  $\sigma_G = 0.02\sigma_i$ ) is added as a random perturbation, where  $\sigma_i$  is  
202 the height-dependent standard deviation of the variable considered. The perturbation is added to

203 ensure that turbulent fields will not be identical whilst keeping the averaged state unchanged. This  
204 is done for all three velocity components and the temperature. The simulation is restarted on the  
205 bigger domain with new domain sizes  $L_x = 96$  m,  $L_y = 38.4$  m and  $L_z = 19.2$  m, and is allowed  
206 to freely evolve for 2 simulation hours. Only the second simulation hour is used for the analysis  
207 as the first simulation hour may be influenced by initial correlation between the individual field  
208 copies. As multiple wave cycles have passed during the first hour, it is assumed that these ‘memory  
209 effects’ of the artificial initialization have disappeared after the first hour (cf. Fig. 2). The grid  
210 spacing is kept at 0.08 m. The extended simulation results in a wavenumber bin resolution of  
211  $\Delta k_x = 0.065 \text{ m}^{-1}$  in the  $x$ -direction (along the isobar) after application of the Fourier transform.

212 Figure 3 shows the perturbation of the  $x$ -component of the velocity  $u'$  at different times dur-  
213 ing a full cycle. Here, the velocity perturbation is defined as the difference between the local,  
214 instantaneous velocity and the horizontally-averaged value. It is observed that at the top of the  
215 boundary layer with height of approximately 2.7 m, a wave pattern of alternating positive and neg-  
216 ative velocity perturbations forms (cf. Fig 3b). Subsequently, the wave amplitude grows in time  
217 and eventually breaks triggering more (vertical) turbulent mixing, which leads to an increase of the  
218 turbulent boundary layer (cf. Fig 3c,d). During the later stages of the event, the wave patterns have  
219 disappeared and the boundary layer has grown to approximately 5.5 m with overall increased val-  
220 ues of the velocity perturbation indicating an increase in turbulent activity (see Fig 3e,f). Finally,  
221 the turbulent activity at the top of the boundary layer dissipates, and the boundary-layer returns  
222 to its pre-burst state (Fig 3g). Similar evolutions are observed for the perturbations of the cross-  
223 isobaric velocity component  $v'$ , the vertical velocity component  $w'$  and the potential temperature  
224  $\theta'$  (not shown).

225 To determine the dominant wavelength, the stages similar to Fig. 3b are selected from the final  
226 three events (out of a total of 4) and analyzed. The first bursting event in the second simulation

227 hour is discarded since it may be influenced by a secondary event (cf. Fig. 2a). Using a similar  
 228 approach as Newsom and Banta (2003), the normalized power spectra at each height  $z$  are com-  
 229 puted by taking the one-dimensional Fourier transform in the  $x$ -direction of each cross section.  
 230 Individual spectra are added and normalized by its maximum value. The Fourier components of  
 231 the perturbation of a variable are indicated by the hat-symbol. For example,  $\hat{\theta}_k$  refers to the Fourier  
 232 component at wavenumber  $k_x \equiv 2\pi/\lambda_x$  (with  $\lambda_x$  the wavelength in the  $x$ -direction;  $k$ th mode) of  
 233 the perturbation in the potential temperature  $\theta'$ .

234 Figure 4 presents the normalized power spectra of both the vertical velocity component  $\hat{w}_k$  and  
 235 potential temperature  $\hat{\theta}_k$  as a function of both height  $z$  and wavenumber  $k_x$ . For clarity, only  
 236 wavenumbers up to  $k_x = 1 \text{ m}^{-1}$  are shown (out of a maximum of  $k_x = 39.22 \text{ m}^{-1}$ ) as the power at  
 237 higher wavenumbers is negligible. The spectra of  $\hat{w}_k$  and  $\hat{\theta}_k$  have their maxima at  $k_x = 0.3274 \text{ m}^{-1}$   
 238 and  $z = 4.36 \text{ m}$ , and at  $k_x = 0.3929 \text{ m}^{-1}$  and  $z = 3.08 \text{ m}$ , respectively. The location of the maximum  
 239 of  $\hat{w}_k$  corresponds to a wavelength of  $\lambda_x = 19.2 \text{ m}$ , while the location of the maximum of  $\hat{\theta}_k$   
 240 corresponds to  $\lambda_x = 16.00 \text{ m}$ . Hence, this analysis confirms the aforementioned visual inspection.

241 Both power spectra have an approximately equal horizontal extent. This indicates that the wave  
 242 phenomenon is composed of multiple wavelengths in a narrow range. The vertical extent of the  
 243 power spectrum of  $\hat{w}_k$  appears to be larger than that of  $\hat{\theta}_k$ . No explanation is found for this dif-  
 244 ference in height of the distribution. The vertical profiles of the power spectra at the dominant  
 245 wavenumber are shown in Fig. 5a,b.

246 Visual inspection of the simulation field at  $t = 5100 \text{ s}$  shows that propagation direction of the  
 247 primary wave events is  $\phi \approx 0^\circ$  with respect to the isobars; that is, aligned with the  $x$ -axis (not  
 248 shown). For convenience, it is therefore taken as  $0^\circ$ . Unfortunately, no value of the complex phase  
 249 speed can be calculated due to the limited frequency at which cross sections and simulation fields  
 250 were saved, namely, 30 s and 300 s, respectively.

251 *b. Linear stability analysis*

252 Linear stability analysis provides information about the hydrodynamic stability of small pertur-  
253 bations (indicated by the prime) subject to a given background flow. Arbitrarily-shaped perturba-  
254 tions of small amplitude are typically present in ‘quiescent’, non-turbulent background flows, and  
255 can be seen as a superposition of sinusoidal waves (Fourier decomposition). By LSA, one inves-  
256 tigate if these wave components (modes) decay or grow in time (i.e., have a negative or positive  
257 growth rate). If all modes contained in the Fourier decomposition decay, the flow is said to be  
258 stable. However, if a number of modes grow (exponentially in time), it is assumed that the fastest  
259 growing mode of these will rapidly dominate over the others and continue to grow until secondary  
260 instability mechanisms cause that wave to break and overturn. An extensive overview on LSA can  
261 be found in Drazin and Reid (2004) and Kundu et al. (2012). Although LSA is traditionally used to  
262 investigate the stability of strictly laminar flows and predict their transition to turbulence (Kundu  
263 et al. 2012), the LSA approach has been stretched in its assumptions by applying it to flows that  
264 are not completely laminar, but are ‘smooth’ with respect to their very weak turbulent activity.  
265 In those cases, LSA is used to analyze whether the mean flow (in a Reynolds-averaged sense)  
266 supports unstable wave modes that will lead to turbulence of more significant magnitude. Indeed,  
267 LSA has been employed with success to predict shear-generated instabilities in the ‘smooth’, but  
268 weakly-turbulent SBL using the observed mean states (see, e.g., Finnigan et al. 1984; de Baas and  
269 Driedonks 1985; Newsom and Banta 2003).

270 1) METHOD

271 Here, we briefly explain the implementation of the LSA. A detailed description can be found in  
272 Appendix B. First, it is assumed that, at a given time, the wave perturbations propagate along one  
273 direction in the horizontal plane. This reduces the 3D problem to a 2D approximation. Note that,

274 this assumption excludes the Coriolis force from the analysis. This simplification is motivated by  
 275 the magnitude of the perturbation Coriolis term after linearization, which is negligible compared  
 276 to the other terms. Second, we assume the flow to be inviscid. The velocity vector is then rotated  
 277 over angle  $\phi$ , which corresponds to an alignment of the flow with the propagation direction (here,  
 278  $\phi \approx 0^\circ$ , section 3a). The mean 2D background states of wind speed and temperature are given  
 279 by  $\mathbf{U} = \{U(z), 0\}$  and  $\Theta(z)$ , respectively. Travelling-wave solutions are assumed for the wave  
 280 disturbances. For example, for the vertical velocity component

$$\begin{aligned}
 w' &= \sum_k w'_k = \text{Re} \left( \sum_k \hat{w}_k(z) e^{ik(x-c_k t)} \right) \\
 &= \text{Re} \left( \sum_k \hat{w}_k(z) e^{ikx} e^{\sigma_k t} \right),
 \end{aligned} \tag{1}$$

281 where  $k$  is the wavenumber,  $\hat{w}_k(z)$  is the complex amplitude (profile) of the  $k$ th mode,  $c_k = c_{k,R} +$   
 282  $ic_{k,I}$  is the complex phase speed. Additionally,  $\sigma_k = -ikc_k$  is introduced for convenience. For a  
 283 mode to be unstable, the real part of  $\sigma_k$  has to be  $> 0 \text{ s}^{-1}$ . Our LSA model investigates the stability  
 284 of a single mode solving for the unknown  $\sigma_k$ , and the corresponding profiles of the vertical velocity  
 285 and temperature perturbations for a given  $k$  and  $\phi$  of that mode. Apart from these, boundary  
 286 conditions for the vertical velocity component have to be specified. Here, we require that the  
 287 vertical velocity component is zero at the bottom ( $\hat{w}_k = 0$ ; no-penetration) and that the solution  
 288 remains bounded for infinite height (viz.,  $\hat{w}_k$  tends to a constant value). The latter boundary  
 289 condition is approximated by  $\frac{d\hat{w}_k}{dz} = -k\hat{w}_k$  at the top of the computational domain. This condition  
 290 automatically ensures that the solution has an exponential decrease to zero at infinite height, while  
 291 recognizing that the actual boundary condition is imposed at finite height. Note that, both  $\frac{d^2 U}{dz^2}$  and  
 292  $\frac{d\Theta}{dz}$  tend to zero here (cf. de Baas and Driedonks 1985; Newsom and Banta 2003). The equation for  
 293 the temperature perturbation can be eliminated by further substitution and would yield the classical

294 Taylor–Goldstein equation (see, e.g., Newsom and Banta 2003), which is a second-order equation  
295 in  $\hat{w}_k$  requiring two boundary conditions. Here, this elimination is not done for convenience.

296 The system of equations is discretized in the vertical direction using  $N_z$  levels (the same as  
297 in the simulation), and transformed into a generalized eigenvalue problem with eigenvalue  $\sigma_k$  and  
298 eigenvector  $[\hat{\mathbf{w}}_k, \hat{\boldsymbol{\theta}}_k]^T$ . Solving the generalized eigenvalue problems gives  $2N_z$  pairs of eigenvalues  
299 and eigenvectors of which  $N_z$  are independent. For each pair, its complex conjugate is also a valid  
300 solution with opposite growth rate (Kundu et al. 2012). The most unstable eigenvalue-eigenvector  
301 pair (largest  $\text{Re}(\sigma_k)$ ) is selected as it is expected to dominate the flow evolution.

## 302 2) RESULT

303 We investigate the stability of waves with wavenumber and propagation direction set equal to  
304  $k = 0.3929 \text{ m}^{-1}$  and  $\phi = 0^\circ$ , respectively (see section 3a). The background profiles of wind speed  
305 and temperature are obtained by averaging the simulated profiles between  $t = 5400$  and  $t = 5700$  s  
306 from the extended domain simulation. This interval is approximately halfway between two suc-  
307 cessive bursts (based on the 2.72-m temperature flux) and is representative of the base state. The  
308 background wind speed profile is then projected onto the plane of propagation, which corresponds  
309 to setting  $U(z) = u(z)$  in our case. Using these parameters, this investigated mode is found to have  
310 the fastest growing eigenvalue  $\sigma_k = (0.0195 - 0.7899i) \text{ s}^{-1}$ . This corresponds to complex phase  
311 speed components of  $c_{k,R} = 2.01 \text{ m s}^{-1}$  and  $c_{k,I} = 0.05 \text{ m s}^{-1}$  (see Fig. B1), where the subscripts ‘*R*’  
312 and ‘*I*’ represent the real and imaginary parts, respectively. The wave speed  $c_{k,R}$  equals the speed  
313 of the background flow at  $z \approx 2.92 \text{ m}$ , so that the midplane of the wave does not move in a coordi-  
314 nate system moving with that flow speed. The  $e$ -folding timescale for exponential growth is  $\approx 51 \text{ s}$   
315 (i.e.,  $k^{-1} c_{k,I}^{-1}$ ). Although this timescale cannot be accurately determined from the simulations due  
316 to the limited output frequency of the cross sections, it appears to be reasonable compared to the

317 timescale of the bursting event (cf. Fig. 2b). A strict comparison is not possible as the linear  
 318 growth regime is violated relatively soon due to fast growth of the wave.

319 Figure 5 shows the normalized wave mode profiles of the vertical velocity component, tempera-  
 320 ture, vertical wave momentum flux and vertical wave temperature flux at the dominant wavenum-  
 321 ber  $k = 0.3929 \text{ m}^{-1}$  as inferred from the simulation (blue) and calculated by the LSA (red). Here,  
 322 the vertical ‘fluxes’, resulting from the temporal growth of the wave amplitude, are calculated as  
 323 the real part of the product of the variable considered and the complex conjugate of the vertical  
 324 velocity component  $\hat{w}_k^*$  (cf. Newsom and Banta (2003)). This product is the generalization of the  
 325 dot product for complex numbers. For temperature, this product represents that part of the temper-  
 326 ature perturbation that is in phase with the perturbation of the vertical velocity component. Note  
 327 that, for non-growing (linear) waves ( $\text{Re}(\sigma_k) = 0 \text{ s}^{-1}$ ) this product is zero (viz.,  $\hat{\theta}_k$  lags  $90^\circ$  with  
 328 respect to  $\hat{w}_k$ ), and, as such, no scalar or momentum is transported. However, for growing waves  
 329 this product is non-zero. Physically, the vertical velocity does not change sign at the moment the  
 330 densest (lightest) fluid is displaced through the midplane in a wave of which the amplitude grows  
 331 in time. The presence of an in-phase component (non-zero product) follows from the LSA model  
 332 equations (see Eq. B7b, Appendix B)

$$\hat{\theta}_k = \frac{i}{k} \left( \frac{d\Theta}{dz} \right) \hat{w}_k, \quad (2)$$

333 which shows that  $\text{Re}(\hat{\theta}_k \hat{w}_k^*) \neq 0$  if and only if  $\text{Im}(c_k) \neq 0$ .

334 The calculated LSA-profiles resemble those estimated from the simulation for all four variables  
 335 to a high degree. Minor differences are mainly found near the surface, which are likely caused  
 336 by some irregular motion (weak turbulence) of minor amplitude. The LSA-calculated profile for  
 337  $||\hat{w}_k||$  smoothly tends toward zero near the top of the domain, whereas the profile estimated from  
 338 the simulations does not. Because turbulent activity is virtually absent in the upper half of the

339 domain (cf. Fig. 1), this might indicate some wave activity there (possibly caused by minor  
340 reflections). As such, the domain is not large enough to fully exclude boundary effects, although  
341 these effects are believed to be minor.

342 A local minimum of  $||\hat{w}_k||$ , and the maxima of  $||\hat{\theta}_k||$  and the wave fluxes are present at  $z = 2.88$  m  
343 coinciding with the inflection point of the velocity profile  $U(z)$ . This height is a critical level of  
344 the flow: the real part of the phase speed  $c_{k,R}$  is equal to the local horizontal velocity at this height.  
345 The large, narrow peaks of the wave momentum and temperature fluxes indicate that large parts  
346 of  $\hat{u}_k$  and  $\hat{\theta}_k$  are in phase with  $\hat{w}_k$  at this height, whereas they are out of phase near the surface and  
347 above the SBL (see Fig. 5c,d).

348 The profiles correspond to those found by de Baas and Driedonks (1985) (vertical velocity and  
349 temperature) and Newsom and Banta (2003) in a non-dimensional form. The shape and struc-  
350 ture of these profiles are consistent with a Kelvin–Helmholtz-type instability (Newsom and Banta  
351 2003). This confirms that the wave formation and wave breaking (cf. Fig. 3) are indeed the result  
352 of a shear instability at the top of the SBL.

#### 353 4. Mechanism behind the full cycle

354 In spite of the close correspondence between the LSA and the simulation results, the previous  
355 section merely confirms that the background flow is unstable for perturbations at the dominant  
356 wavenumber. It does, however, not reveal how the boundary layer responds during the burst and  
357 relaxes back to its base state. In this section, this process is analyzed by conditional averaging  
358 over the bursting and the non-bursting periods. First, the effect of the intermittent burst on the  
359 mean flow is shown. Second, the evolution of the boundary layer after a burst is presented and, in  
360 particular, it is revealed why the process of shear-generated intermittent bursts is periodic.

361 *a. Flow evolution during the burst*

362 Figure 6 shows the flux profiles of momentum  $F(u_i)$  and temperature  $F(\theta)$ , and the contribu-  
363 tions to the tendencies of the isobaric velocity component  $u$  and temperature  $\theta$ . These values are  
364 conditionally averaged on the bursting states taken from the final simulation hour of the original  
365 VSBL simulation (see van der Linden et al. 2019). These contributions for  $u$  are the divergence  
366 of the total isobaric momentum flux and the  $x$ -component of the Coriolis force, whereas the con-  
367 tributions for  $\theta$  are the divergence of the kinematic temperature flux and heating by subsidence.  
368 The  $x$ -component of the Coriolis force is given by  $f_C v$ . This term does not ‘add’ momentum (or  
369 energy) to the flow as the Coriolis force is always perpendicular to the wind vector. However, it  
370 can rotate the wind vector thereby transferring momentum (and energy) from the  $y$ -direction to  
371 the  $x$ -direction (and vice versa) in the case of a force imbalance. At the same time, the imposed  
372 pressure gradient force steadily adds momentum to the cross-isobaric direction ( $y$ -direction). The  
373 bursting (non-bursting) state is defined as those time intervals in which the absolute value of the  
374 2.72-m temperature flux is larger (smaller) than the absolute value of the surface temperature flux  
375 (cf. Fig. 2b). The total fraction of the time the SBL resides in the bursting (non-bursting) state is  
376 26% (74%).

377 Both the isobaric momentum flux ( $x$ -direction) and temperature flux exhibit large negative peaks  
378 centred around 2.72 m (cf. Fig. 5) exceeding the surface values. The averaged vertical extent of  
379 the peaks is approximately equal to 4 m and is dependent on the time during the burst: after the  
380 initial wave breaks, momentum and heat are progressively mixed in the vertical direction. As a  
381 result of the burst, turbulent kinetic energy is generated and the boundary-layer height increases  
382 up to  $\approx 5.5$  m. Additionally, the base state becomes temporarily ‘coupled’ to the layer above.

383 The  $x$ -component of the Coriolis force  $f_{Cv}$  and the heating by subsidence both have a positive  
384 contribution to the tendencies of  $u$  and  $\theta$ , respectively, and tend to zero for  $z > 6$  m (see Fig. 6c,d).  
385 The contributions as a result of the flux divergences show a more complicated pattern: they are  
386 mainly positive in the lower layer and negative higher up. In total, a net acceleration and warming  
387 of the SBL occur below  $\approx 2.9$  m, whereas in the region 3–5 m (relatively) strong deceleration and  
388 cooling occur. The vertical transport by bursting, hence, reduces both the difference in the velocity  
389 magnitude and the temperature between the upper and lower layer. As the relative decrease of the  
390 shear is larger than the decrease in thermal gradient, the cause of instability is counteracted (see  
391 Fig. 8).

392 In addition to the isobaric velocity component, also changes in the cross-isobaric component  
393 occur. Although the profile of the total rate-of-change of the cross-isobaric velocity component  
394 exhibits a more complicated structure, its values are typically  $< 50\%$  of the total rate-of-change of  
395  $u$  and have a relative small contribution to the change of the total shear squared  $S^2$  (not shown).

#### 396 *b. Flow evolution after the burst*

397 In the non-bursting state, the flux and total rate-of-change profiles are markedly different than in  
398 the bursting state (see Fig. 7). The profiles of the momentum and temperature fluxes indicate that  
399 the main turbulent layer is now approximately 3 m in depth.

400 It is found that the profiles of the  $x$ -component of the Coriolis force  $f_{Cv}$  and the heating by  
401 subsidence do not significantly differ in the non-bursting state as compared to the bursting state.  
402 The figures, however, do differ with respect to the turbulent flux contributions (see Fig. 7c,d).  
403 In absence of momentum and heat transport from above, the lower layer ( $z < 3$  m) decelerates  
404 due to the surface friction (momentum flux divergence) and cools by the surface temperature  
405 flux (temperature flux divergence). This lower layer corresponds to the active turbulent layer in

406 the non-bursting state, whereas the layer above can be regarded as ‘quasi-laminar’. At the same  
407 time, this quasi-laminar layer experiences a net acceleration and warming by the Coriolis force  
408 and subsidence heating. The overall result is that the contrast between the lower and the upper  
409 layer increases with respect to the wind speed and temperature (i.e., an increase of the local shear  
410 and temperature gradient around  $z \approx 3$  m). The momentum transferred from the cross-isobaric  
411 to the isobaric direction by the Coriolis force is steadily replenished by the pressure force in the  
412 y-direction (not shown).

413 Weighted by their respective fractions of occurrence, the deceleration and cooling, and the ac-  
414 celeration and warming balance in time. As such, both a steady state in the amount of momentum  
415 and a thermal steady state result, when averaged over, for example, times  $> 1$  h (see van der Linden  
416 et al. 2019; their Fig. 8). The intermittent bursts of the SBL, therefore, contribute to this thermal  
417 steady state in the presence of heating by subsidence. Periodically, they ‘entrain’ relatively warm  
418 air heated by subsidence into the turbulent layer. Mirocha et al. (2005) already provided com-  
419 pelling evidence that warm air entrained into the boundary layer by subsiding motions balances  
420 a significant part of the turbulent heat flux near the surface in the observed Arctic clear-sky SBL.  
421 Similarly, a LES case based on this Arctic SBL (Mirocha and Kosović 2010) shows that the in-  
422 clusion of subsidence resulted in a nearly thermal steady state. However, they did not report any  
423 (periodic) bursts within the SBL.

424 The impact of the bursting and the non-bursting phases on the mean quantities are summarized  
425 in Fig. 8. This figure shows the profiles of the total shear squared  $S^2$ , Brunt–Väisälä frequency  
426  $N^2$  and the gradient Richardson number  $Ri_g = N^2 S^{-2}$  representative of different times during one  
427 cycle (just before a burst and after the burst) of the original VSBL simulation. The temporal  
428 variation in  $S^2$  and  $N^2$  result in clear changes of  $Ri_g$  over the shear layer during a cycle. Finally, a  
429 conceptual picture of the mechanism and its main actors are given in Fig. 9.

## 430 5. Discussion

### 431 a. Comparison with suggested mechanisms

432 The current results suggest a systematic mechanism by which cyclic intermittent bursts are trig-  
433 gered by a Kelvin–Helmholtz instability at the interface of a shallow SBL and the quasi-laminar  
434 layer above. Similar mechanisms (or parts thereof) have been reported in literature. Yet, a com-  
435 prehensive, observationally-based explanation by which multiple intermittent bursts may occur  
436 successively or even periodically within an uninterrupted timespan has not been given (Mahrt  
437 2014). Indeed, systematic observations of such successive bursts may be difficult due to both  
438 observational limitations and non-stationarity of the SBL itself in the mid-latitudes.

439 The mechanism identified in this study resembles the mechanism reported by Newsom and Banta  
440 (2003). They show that, just prior to the burst, the shear dominates the reduction of the Richardson  
441 number causing the flow to become locally unstable. In particular, the build-up of shear over a  
442 relatively small vertical extent triggers a Kelvin–Helmholtz instability. Furthermore, they find a  
443 net increase of  $Ri$  during the wave event as both shear and temperature gradient are mixed, and a  
444 small decrease of  $Ri$  after the wave event for which no cause is identified. This observation appears  
445 to correspond with our simulations, although a direct comparison is difficult due to observational  
446 limitations (e.g., determining gradients from discrete levels) and the number of events (1 in their  
447 case).

448 Also, similarities and dissimilarities between the mechanism of van de Wiel et al. (2002) and  
449 the current mechanism are present. Van de Wiel et al. (2002) acknowledge the potential role  
450 of the ageostrophic pressure gradient (i.e., the effective pressure gradient in the direction of the  
451 mean wind) as a main external parameter governing intermittency in their bulk model. The main  
452 difference, however, is that their bulk model cannot capture the instability and the dynamics at the

453 interface of the SBL and the quasi-laminar layer above, but considers a suppression of the turbulent  
454 activity of the SBL as a whole (governed by the bulk Richardson number). The present results,  
455 on the contrary, provide compelling evidence for a two-layer structure with separate dynamics:  
456 whereas no turbulence is present above the interface and the flow accelerates there, the SBL itself  
457 decelerates as a result of the surface friction in the non-bursting state. As such, it appears that the  
458 mechanism of van de Wiel et al. (2002) is less realistic. At the same time, our simulation imposes  
459 a fixed surface temperature via the boundary condition, whereas, in van de Wiel et al. (2002) the  
460 thermal balance of the surface is an active (dynamic) part of the system, which may allow for  
461 additional surface feedbacks not considered here.

462 Finally, the mechanism found in this study is remarkably close to the conjecture of Businger  
463 (1973). Here, we cite parts of his conjecture:

464 *“The point is that if  $R_{fcr}$  is reached sometime . . . , it will be reached first where the maximum*  
465 *value occurs at some height above, but relatively close, to the surface. As soon as this happens*  
466 *the turbulence will be dampened and a laminar layer will tend to form. This layer is an effective*  
467 *barrier for all the fluxes. . . . Under the laminar layer the transfer of momentum will continue*  
468 *down to the surface until the available momentum is depleted or  $R_f$  has become larger than*  
469 *critical. The result is that the wind diminishes and a period of calm sets in. . . . In the meantime,*  
470 *above the laminar layer momentum is still transferred downward whereas little heat is transferred.*  
471 *Consequently, the momentum increases in the upper part of the laminar layer because it cannot*  
472 *pass through this layer. A strong wind shear builds up and since there is no similar effect for the*  
473 *heat flux,  $Ri$  must decrease, eventually reaching a value below  $Ri_{cr}$ . This means that the laminar*  
474 *layer will gradually be eaten away by turbulence from above. Eventually the turbulence reaches*  
475 *the ground associated with a burst of momentum and heat. After this, the entire sequence of events*  
476 *may repeat itself.”*

477 However, the key difference is the actor that increases the momentum above the boundary layer  
478 during the non-bursting times. Whereas Businger suggested that momentum is transferred down-  
479 wards from higher up in the flow by stress convergence, the current results indicate momentum is  
480 increased by acceleration as a result of the pressure gradient and subsequent rotation by the Cori-  
481 olis force, which are a rather constant factor in time. Apart from this difference, his conjecture is  
482 correct with regard to the origin of the burst, the deceleration in the bulk of the SBL and the possi-  
483 bility of periodicity. Finally, we acknowledge the fact that our studied long-lived ABL may differ  
484 from the mid-latitude diurnal ABL, where additionally the nocturnal momentum budget might be  
485 influenced by, e.g., decaying convection and inertial oscillations.

486 *b. A systematic climatology of bursts?*

487 The present study would largely benefit from a systematic climatology of bursts. Such clima-  
488 tology may clarify under which conditions successive or even periodic bursting events can occur.  
489 In our simulations, the external forcings (e.g., the geostrophic wind speed and subsidence profile)  
490 are kept constant, and the surface is homogeneous. As a result, the simulation reaches a steady  
491 state in which the bursts only marginally affect the background flow allowing a fast recovery and  
492 subsequent burst. A strict steady state is not expected to occur in the outdoor environment in which  
493 synoptic disturbances occur, but may be approached for several days in the polar regions.

494 Petenko et al. (2019) show that periods lasting several hours in which the SBL is perturbed by  
495 successive wave events, are frequent at the Dome C station (see their Fig. 9). They note that the  
496 large-scale weather conditions were stationary during these periods. However, the lack of accu-  
497 rate turbulent flux measurements (e.g., using eddy-covariance techniques) and the limited amount  
498 of measurement levels on the meteorological tower prevent the determination of the interactions  
499 between the mean flow and the wave events.

500 Another open question relates to the climatology of the event in relation to external forcings.  
501 In contrast to the present study, Petenko et al. (2019) seem to suggest that intermittency is more  
502 likely to occur within SBLs of depth 20–70 m than in very shallow SBLs of depth  $z \approx 5$  m. This im-  
503 plies a larger geostrophic forcing (i.e., near-surface large-scale pressure gradient), and/or a weaker  
504 subsidence warming as to allow a larger turbulent activity and a deeper SBL. At the same time,  
505 however, the timescales of successive event in their study corresponds to the timescale identified  
506 in the present study: 8–15 min in theirs as compared to 10 min in the current. Therefore a one-to-  
507 one comparison of intermittency climatology with respect to forcings between observations and  
508 modelling is essential in order to generalize the present conclusions.

## 509 6. Conclusions

510 In this study, a mechanism for periodic shear-generated intermittent bursts is identified using  
511 high-resolution LES. This mechanism closely resembles the mechanism proposed by Businger  
512 (1973) differing only in the cause of acceleration above the SBL.

513 Van der Linden et al. (2019) simulate the VSBL based on observations of the Antarctic winter  
514 of 2015 from the Dome C station in related work. They show that the temperature flux divergence  
515 and heating by subsidence balance over timescales  $> 1$  h such that a steady-state SBL with depth  
516  $\approx 5.5$  m is reached. Here, we find that the SBL is not in steady state over timescales  $< 10$  min, but  
517 is rather modulated by turbulent bursts, which enable the steady state over longer timescales.

518 Using an extended simulation domain, it is found that periodically wave perturbations form at  
519 the interface of a shallow SBL (2.5–2.9 m) and a quasi-laminar layer above (i.e., flow with negli-  
520 gible turbulent activity). The dominant wave is found to grow in time until it breaks resulting in  
521 increased turbulent activity and a temporary growth of the active turbulent layer. Spectral analysis  
522 shows that the wavelength of this dominant wave is 16–19 m.

523 A linear stability analysis confirms that small-amplitude waves of this wavelength are indeed  
524 unstable with respect to the mean wind and temperature profiles. Furthermore, the predicted  
525 perturbation profiles of the velocity components, temperature and fluxes correspond with those  
526 obtained by the spectral analysis. The shape of these perturbation profiles are indicative of the  
527 Kelvin–Helmholtz instability, which has been found to occur before in stable conditions (see, e.g.,  
528 de Baas and Driedonks 1985; Newsom and Banta 2003).

529 The instability is created by an increase of the local shear at the interface that dominates over  
530 the increase in temperature gradient resulting in a decrease of  $Ri_g$  to a value  $< 0.25$ , which is a  
531 prerequisite for instability to occur (see, e.g., Kundu et al. 2012). The interfacial shear is increased  
532 as a result of deceleration of the flow in the SBL by turbulent friction, and acceleration above by  
533 the combined action of the pressure forcing and the rotation by the Coriolis force. During the  
534 burst, these two layers become temporarily coupled and the momentum is exchanged; that is, the  
535 lower part accelerates and the higher part decelerates. The instability is mixed away by its own  
536 result and  $Ri_g$  becomes  $> 0.25$  at the interface. It is found, however, that the mean wind is only  
537 altered slightly by the burst and returns to its pre-burst state. As such, the flow is found to reside  
538 around its critical state, and a cyclic process of instability formation and bursting ensues. This is a  
539 (modified) Businger mechanism. Businger (1973) correctly proposed such intermittency could be  
540 periodic by the process described above with one exception. He stated that the momentum above  
541 the SBL is increased due to downward turbulent transfer. However, such transfer is not possible  
542 as a result of negligible turbulent activity above the SBL. It is important to note that, apart from  
543 turbulence, the potential impact of subsidence on the momentum budget is not considered in the  
544 present study, which can result in an additional supply of momentum.

545 The temperature dynamics follow a similar pattern. Prior to the burst, the SBL is cooled by the  
546 turbulent flux toward the surface and the quasi-laminar layer is heated by the subsidence heating.

547 During the burst, the cooler air is mixed upward and the warmer air is mixed downward. It is this  
548 periodic mixing that explains the thermal steady state over timescales  $> 1$  h reported by van der  
549 Linden et al. (2019).

550 Although intermittent bursts are commonly observed in the SBL at both the mid- and high-  
551 latitudes, the exact conditions leading to such bursts, and, in particular, successive (periodic) bursts  
552 remain elusive. At the same time, while the steady forcing conditions of the simulation allow  
553 periodic bursts to occur and the mechanism to be revealed, these conditions are just one realization  
554 of the SBL based on observations from the Antarctic winter and a sensitivity study in which these  
555 conditions, such as, the geostrophic wind speed, are systemically varied is recommended. A  
556 detailed climatology of shear-generated bursts in relation to the conditions in which they are found  
557 (e.g., mean wind or surface characteristics) would therefore be beneficial, and help to predict the  
558 timescales and vertical extent of such bursts among other things. Furthermore, realistic high-  
559 resolution simulations based on such climatological cases can clarify the contribution of bursts to  
560 vertical transfer of momentum and scalars.

561 *Acknowledgments.* This work was sponsored by NWO Exact and Natural Sciences for the use of  
562 supercomputer facilities. We gratefully acknowledge funding by the European Research Council  
563 through an ERC-Consolidator grant (648666).

## 564 APPENDIX A

### 565 **Description of the LES case**

566 In the current study, the LES case for the VSBL of van der Linden et al. (2019) is used. Here, we  
567 briefly summarize the set-up of their VSBL simulation. A detailed description of the observations,

568 set-up and results can be found in van der Linden et al. (2019). Furthermore, the used, open-source  
569 code MicroHH (<http://microhh.org>) is described in van Heerwaarden et al. (2017).

570 The subfilter-scale flux tensors are modelled by a Smagorinsky–Lilly-type eddy-viscosity model  
571 (Lilly 1962; Smagorinsky 1963) in which stratification effects are included (Lilly 1962; Mason  
572 1989). Furthermore, the wall-correction of Mason and Thomson (1992) is used for the length  
573 scale of the eddy-viscosity. Surface fluxes are calculated using Monin–Obukhov Similarity Theory  
574 with the similarity functions of Högström (1988). Velocity boundary conditions for the horizontal  
575 components are no-slip at the surface and stress-free at the top, and no-slip at both surface and  
576 top for the vertical velocity. For temperature, Dirichlet conditions are used. Heating of the air by  
577 subsidence is calculated as the product of a constant linear subsidence profile (zero at the surface)  
578 and the domain averaged temperature gradient. Subsidence of momentum is not included in the  
579 current work for simplicity. However, it would be interesting to assess its potential impact on the  
580 intermittency mechanism in future work.

581 Simulations are initialised with constant temperature  $\theta_0$  and constant velocity  $(G, 0, 0)$  in the  $x$ -,  
582  $y$ - and  $z$ -directions, respectively. At the start of the simulation, the surface is cooled by 25 K after  
583 which cooling is stopped, and the simulation is continued to reach steady state. An overview of  
584 the parameters used in the VSBL case is given in Table 6.

## 585 APPENDIX B

### 586 Derivation of the LSA

587 We consider the conservation equation of mass, the inviscid Navier–Stokes equation and the con-  
588 servation equation of energy (written in temperature form) under the Boussinesq approximation in

$$\partial_i u_i = 0, \quad (\text{B1a})$$

$$\partial_t u_i = -u_j \partial_j u_i + \frac{g}{\theta_0} (\theta - \theta_0) \delta_{i3} - \partial_i p, \quad (\text{B1b})$$

$$\partial_t \theta = -u_j \partial_j \theta, \quad (\text{B1c})$$

590 where  $u_i$  are the velocity components in the  $x$ - and  $z$ -direction,  $\theta$  is the potential temperature,  $\theta_0$   
591 is the reference temperature,  $g$  is the acceleration due to gravity and  $p$  is the modified pressure.

592 We assume that our variables can be decomposed into their mean background states and a con-  
593 tribution due to perturbations indicated by a capital letter and a prime, respectively,

$$u(x, z, t) = U(z) + u', \quad (\text{B2a})$$

$$w(x, z, t) = w', \quad (\text{B2b})$$

$$\theta(x, z, t) = \Theta(z) + \theta', \quad (\text{B2c})$$

$$p(x, z, t) = p'. \quad (\text{B2d})$$

594 These expressions are inserted into Eq. B1 and subsequently the mean state balance is sub-  
595 tracted. Additionally, products of perturbed quantities are assumed to be negligibly small and  
596 therefore removed. This results in a new set of *linearized* equations for the perturbed variables

$$\partial_x u' + \partial_z w' = 0, \quad (\text{B3a})$$

$$\partial_t u' = -U(z) \partial_x u' - w' \frac{dU}{dz} - \partial_x p, \quad (\text{B3b})$$

$$\partial_t w' = -U(z) \partial_x w' + \frac{g}{\theta_0} \theta' - \partial_z p, \quad (\text{B3c})$$

$$\partial_t \theta' = -U(z) \partial_x \theta' - w' \frac{d\Theta}{dz}. \quad (\text{B3d})$$

597 By taking the derivatives of Eq. B3b and B3c with respect to  $x$  and  $z$ , respectively, adding them  
 598 and applying Eq. B3a, a Poisson equation for the pressure is obtained

$$\nabla^2 p' = -2\partial_x w' \frac{dU}{dz} + \frac{g}{\theta_0} \partial_z \theta'. \quad (\text{B4})$$

599 Subsequently, by taking the Laplacian ( $\nabla^2$ ) of Eq. B3c and the  $z$ -derivative of Eq. B4, the pres-  
 600 sure is eliminated. This results in a reduced set of equations for the vertical velocity perturbation  
 601 and the temperature

$$\partial_t \nabla^2 w' = -U(z) \partial_x \nabla^2 w' + \frac{d^2 U}{dz^2} \partial_x w' + \frac{g}{\theta_0} \partial_{xx} \theta', \quad (\text{B5a})$$

$$\partial_t \theta' = -U(z) \partial_x \theta' - w' \frac{d\Theta}{dz}. \quad (\text{B5b})$$

602 Next, travelling-wave solutions (complex Fourier components) are taken as Ansatz, for example,  
 603 for the vertical velocity (perturbation)

$$\begin{aligned} w' &= \sum_k w'_k = \text{Re} \left( \sum_k \hat{w}_k(z) e^{ik(x-c_k t)} \right) \\ &= \text{Re} \left( \sum_k \hat{w}_k(z) e^{ikx} e^{\sigma_k t} \right), \end{aligned} \quad (\text{B6})$$

604 where  $k$  is the real wavenumber,  $\hat{w}_k(z)$  is the complex amplitude (profile) of the  $k$ th mode,  $c_k =$   
 605  $c_{k,R} + ic_{k,I}$  is the phase speed, and  $\sigma_k = -ikc_k$  is the growth rate. A positive value of  $\text{Re}(\sigma_k)$  (or  
 606  $c_{k,I}$ ) results in a growing wave mode in time indicating instability. Substitution of this Ansatz and  
 607 cancellation of the exponentials leads to (for each wave mode separately)

$$\sigma_k \left( \frac{d^2}{dz^2} - k^2 \right) \hat{w}_k = -ikU(z) \left( \frac{d^2}{dz^2} - k^2 \right) \hat{w}_k \quad (\text{B7a})$$

$$+ ik \frac{d^2 U}{dz^2} \hat{w}_k - \frac{g}{\theta_0} k^2 \hat{\theta}_k,$$

$$\sigma_k \hat{\theta}_k = -ikU(z) \hat{\theta}_k - \frac{d\Theta}{dz} \hat{w}_k. \quad (\text{B7b})$$

608 This set of equations is to be numerically solved for the unknown growth rate  $\sigma_k$ , and the cor-  
 609 responding profiles of the vertical velocity and temperature perturbations. To do this, a finite-  
 610 difference approximation is used in which the amplitude profiles are discretized in  $N_z$  vertical  
 611 levels (i.e.,  $\hat{w}_k(z)$  is discretized as the vector  $\hat{\mathbf{w}}_k$  of finite length  $N_z$ ). This transforms Eq. B5 into  
 612 a generalized eigenvalue problem with eigenvalue  $\sigma_k$  and eigenvector  $[\hat{\mathbf{w}}_k, \hat{\theta}_k]^T$

$$\sigma_k \begin{bmatrix} \mathbf{A} & \mathbf{0} \\ \mathbf{0} & \mathbf{I} \end{bmatrix} \begin{bmatrix} \hat{\mathbf{w}}_k \\ \hat{\theta}_k \end{bmatrix} = \begin{bmatrix} \mathbf{B}_{11} & \mathbf{B}_{12} \\ \mathbf{B}_{21} & \mathbf{B}_{22} \end{bmatrix} \begin{bmatrix} \hat{\mathbf{w}}_k \\ \hat{\theta}_k \end{bmatrix} \quad (\text{B8})$$

613 in which the  $\mathbf{A}$ ,  $\mathbf{B}_{11}$ ,  $\mathbf{B}_{12}$ ,  $\mathbf{B}_{21}$  and  $\mathbf{B}_{22}$  are block matrices of size  $N_z \times N_z$  with  $N_z$  being the amount  
 614 of vertical levels. These block matrices are given by

$$\mathbf{A} = \mathbf{D}^2 - k^2 \mathbf{I}, \quad (\text{B9a})$$

$$\mathbf{B}_{11} = -ik\mathbf{U}^T \mathbf{A} + ik(\mathbf{U}_{zz})^T \mathbf{I}, \quad (\text{B9b})$$

$$\mathbf{B}_{12} = -\frac{g}{\theta_0} k^2 \mathbf{I}, \quad (\text{B9c})$$

$$\mathbf{B}_{21} = -\mathbf{T}_{zz}^T \mathbf{I}, \quad (\text{B9d})$$

$$\mathbf{B}_{22} = -ik\mathbf{U}^T \mathbf{I}, \quad (\text{B9e})$$

615 where  $\mathbf{D}^2$  is the matrix for the finite-difference second derivatives,  $\mathbf{I}$  is the identity matrix, and  $\mathbf{U}$ ,  
 616  $\mathbf{U}_{zz}$  and  $\mathbf{T}_{zz}$  are column vectors (size  $N_z \times 1$ ) of the discretized background velocity magnitude,

617 second derivative of the velocity magnitude and the second derivative of the temperature, respec-  
 618 tively. Note that,  $\mathbf{B}_{12}$ ,  $\mathbf{B}_{21}$  and  $\mathbf{B}_{22}$  are diagonal matrices. The second derivatives are calculated by  
 619 using a second-order central difference scheme.

620 For the configuration in this study, the boundary conditions are  $\hat{w}_k = 0$  at  $z = 0$  and  $\frac{d\hat{w}_k}{dz} = -k\hat{w}_k$   
 621 at  $z = L_z$  (top of the computational domain). The latter is an approximation for  $\hat{w}_k \rightarrow 0$  as  $z \rightarrow \infty$   
 622 (see, e.g., Newsom and Banta 2003), which can be derived from the 2nd-order differential equation  
 623 (Taylor–Goldstein equation) resulting from elimination of the temperature perturbation and using  
 624 the fact that both  $\frac{d^2U}{dz^2}$  and  $\frac{d\Theta}{dz}$  tend to zero above the SBL. These boundary conditions for  $\hat{w}_k$  and  
 625 its first derivative are imposed through modification of  $\mathbf{D}^2$ . The first boundary condition does not  
 626 require a change of  $\mathbf{D}^2$ . The second is implemented by alteration of the trace element and sub-trace  
 627 element:  $D^2(N_z, N_z) = (-2 - 2\Delta_z k)/\Delta_z^2$  and  $D^2(N_z - 1, N_z) = 2/\Delta_z^2$ .

628 Figure B1 shows the growth rate as a function of the wavenumber for the case considered in  
 629 the main text. The wavenumber of the unstable waves in the extended domain simulation as  
 630 identified by the spectral analysis (indicated by the blue dotted line; see section 3a) is close to  
 631 global maximum given by LSA. The difference in predicted growth rate is less than 4%. This  
 632 minor discrepancy may be due to viscosity effects (not considered in the LSA), non-linear growth  
 633 or numerical approximations.

## 634 References

- 635 Acevedo, O. C., and D. R. Fitzjarrald, 2003: In the Core of the Night-Effects of Intermittent  
 636 Mixing on a Horizontally Heterogeneous Surface. *Bound.-Layer Meteor.*, **106** (1), 1–33, doi:  
 637 10.1023/A:1020824109575.
- 638 Baas, P., B. J. H. van de Wiel, E. van Meijgaard, E. Vignon, C. Genthon, S. J. A. van der Linden,  
 639 and S. R. de Roode, 2019: Transitions in the wintertime near-surface temperature inversion at

- 640 Dome C, Antarctica. *Quart. J. Roy. Meteor. Soc.*, **145 (720)**, 930–946, doi:10.1002/qj.3450.
- 641 Banta, R. M., L. Mahrt, D. Vickers, J. Sun, B. B. Balsley, Y. L. Pichugina, and E. J. Williams,  
642 2007: The Very Stable Boundary Layer on Nights with Weak Low-Level Jets. *J. Atmos. Sci.*,  
643 **64 (9)**, 3068–3090, doi:10.1175/JAS4002.1.
- 644 Blumen, W., R. Banta, S. P. Burns, D. C. Fritts, R. Newsom, G. S. Poulos, and J. Sun, 2001:  
645 Turbulent statistics of a Kelvin–Helmholtz billow event observed in the night-time boundary  
646 layer during the Cooperative Atmosphere-Surface Exchange Study field program. *Dyn. Atmos.*  
647 *Oceans*, **34**, 189–204, doi:10.1016/S0377-0265(01)00067-7.
- 648 Bosveld, F. C., P. Baas, E. van Meijgaard, E. I. F. de Bruijn, G.-J. Steeneveld, and A. A. M.  
649 Holtslag, 2014: The Third GABLS Intercomparison Case for Evaluation Studies of Boundary-  
650 Layer Models. Part A: Case Selection and Set-Up. *Bound.-Layer Meteor.*, **152 (2)**, 133–156,  
651 doi:10.1007/s10546-014-9917-3.
- 652 Businger, J. C., 1973: Turbulent Transfer in the Atmospheric Surface Layer. *Workshop on Mi-*  
653 *crometeorology*, D. A. Haugen, Ed., Amer. Meteor. Soc., 67–100.
- 654 Coulter, R. L., 1990: A case study of turbulence in the stable nocturnal boundary layer. *Bound.-*  
655 *Layer Meteor.*, **52 (1)**, 75–91, doi:10.1007/BF00123179.
- 656 Dabberdt, W. F., 1970: A Selective Climatology of Plateau Station, Antarctica. *J. Appl. Meteor.*,  
657 **9 (2)**, 311–315, doi:10.1175/1520-0450(1970)009<0312:ASCOPS>2.0.CO;2.
- 658 de Baas, A. F., and A. G. M. Driedonks, 1985: Internal gravity waves in a stably stratified boundary  
659 layer. *Bound.-Layer Meteor.*, **31 (3)**, 303–323, doi:10.1007/BF00120898.
- 660 Drazin, P. G., and W. H. Reid, 2004: *Hydrodynamic Stability*. 2nd ed., Cambridge Mathematical  
661 Library, Cambridge University Press, 628 pp., doi:10.1017/CBO9780511616938.

- 662 Finnigan, J. J., F. Einaudi, and D. Fua, 1984: The Interaction between an Internal Gravity Wave  
663 and Turbulence in the Stably-Stratified Nocturnal Boundary Layer. *J. Atmos. Sci.*, **41** (16), 2409–  
664 2436, doi:10.1175/1520-0469(1984)041<2409:TIBAIG>2.0.CO;2.
- 665 Gossard, E. E., J. H. Richter, and D. Atlas, 1970: Internal waves in the atmosphere from  
666 high-resolution radar measurements. *J. Geophys. Res.*, **75** (18), 3523–3536, doi:10.1029/  
667 JC075i018p03523.
- 668 Grachev, A. A., E. L. Andreas, C. W. Fairall, P. S. Guest, and P. O. G. Person, 2008: Turbulent  
669 measurements in the stable atmospheric boundary layer during SHEBA: ten years after. *Bound.-*  
670 *Layer Meteor.*, **56** (1), 142–166, doi:10.2478/s11600-007-0048-9.
- 671 Grachev, A. A., C. W. Fairall, P. O. G. Person, E. L. Andreas, and P. S. Guest, 2005: Stable  
672 Boundary-Layer Scaling Regimes: The Sheba Data. *Bound.-Layer Meteor.*, **116** (2), 201–235,  
673 doi:10.1007/s10546-004-2729-0.
- 674 Höglström, U., 1988: Non-dimensional wind and temperature profiles in the atmospheric surface  
675 layer: A re-evaluation. *Bound.-Layer Meteor.*, **42** (1), 55–78, doi:10.1007/BF00119875.
- 676 Kundu, P. K., I. M. Cohen, and D. R. Dowling, 2012: *Fluid Mechanics*. Academic Press, 928 pp.
- 677 Lilly, D. K., 1962: On the numerical simulation of buoyant convection. *Tellus*, **14** (2), 148–172,  
678 doi:10.1111/j.2153-3490.1962.tb00128.x.
- 679 Mahrt, L., 1999: Stratified Atmospheric Boundary Layers. *Bound.-Layer Meteor.*, **90** (3), 375–  
680 396, doi:10.1023/A:1001765727956.
- 681 Mahrt, L., 2014: Stably Stratified Atmospheric Boundary Layers. *Annu. Rev. Fluid Mech.*, **46** (1),  
682 23–45, doi:10.1146/annurev-fluid-010313-141354.

- 683 Mahrt, L., and D. Vickers, 2002: Contrasting vertical structures of nocturnal boundary layers.  
684 *Bound.-Layer Meteor.*, **105** (2), 351–363, doi:10.1023/A:1019964720989.
- 685 Mason, P. J., 1989: Large-Eddy Simulation of the Convective Atmospheric Boundary Layer. *J.*  
686 *Atmos. Sci.*, **46** (11), 1492–1516, doi:10.1175/1520-0469(1989)046<1492:LESOTC>2.0.CO;2.
- 687 Mason, P. J., and D. J. Thomson, 1992: Stochastic backscatter in large-eddy simulations of bound-  
688 ary layers. *J. Fluid Mech.*, **242**, 51–78, doi:10.1017/S0022112092002271.
- 689 Mirocha, J. D., and B. Kosović, 2010: A Large-Eddy Simulation Study of the Influence of Sub-  
690 sidence on the Stably Stratified Atmospheric Boundary Layer. *Bound.-Layer Meteor.*, **134** (1),  
691 1–21, doi:10.1007/s10546-009-9449-4.
- 692 Mirocha, J. D., B. Kosović, and J. A. Curry, 2005: Vertical Heat Transfer in the Lower Atmosphere  
693 over the Arctic Ocean During Clear-sky Periods. *Bound.-Layer Meteor.*, **117** (1), 37–71, doi:  
694 10.1007/s10546-004-1130-3.
- 695 Na, J. S., E. K. Jin, and J. S. Lee, 2014: Investigation of Kelvin–Helmholtz instability in the  
696 stable boundary layer using large eddy simulation. *J. Geophys. Res. Atmos.*, **119**, 7876–7888,  
697 doi:10.1002/2013JD021414.
- 698 Nappo, C. J., 1991: Sporadic breakdowns of stability in the PBL over simple and complex terrain.  
699 *Bound.-Layer Meteor.*, **54** (1), 69–87, doi:10.1007/BF00119413.
- 700 Newsom, R. K., and R. M. Banta, 2003: Shear-Flow Instability in the Stable Nocturnal Boundary  
701 Layer as Observed by Doppler Lidar during CASES-99. *J. Atmos. Sci.*, **60** (1), 16–33, doi:  
702 10.1175/1520-0469(2003)060<0016:SFITS>2.0.CO;2.

- 703 Petenko, I., S. Argentini, G. Casasanta, C. Genthon, and M. Kallistratova, 2019: Stable Surface-  
704 based Turbulent Layer during the Polar Winter at Dome C, Antarctica: Sodar and In-situ Ob-  
705 servations. *Bound.-Layer Meteor.*, **171** (1), 101–128, doi:10.1007/s10546-018-0419-6.
- 706 Smagorinsky, J., 1963: General Circulation Experiments with the Primitive Equations. *Mon. Wea.*  
707 *Rev.*, **91** (3), 99–164, doi:10.1175/1520-0493(1963)091<0099:GCEWTP>2.3.CO;2.
- 708 Sun, J., L. Mahrt, R. M. Banta, and Y. L. Pichugina, 2012: Turbulence Regimes and Turbulence  
709 Intermittency in the Stable Boundary Layer during CASES-99. *J. Atmos. Sci.*, **69** (1), 338–351,  
710 doi:10.1175/JAS-D-11-082.1.
- 711 Sun, J., and Coauthors, 2004: Atmospheric Disturbances that Generate Intermittent Turbu-  
712 lence in Nocturnal Boundary Layers. *Bound.-Layer Meteor.*, **110** (2), 255–279, doi:10.1023/A:  
713 1026097926169.
- 714 van de Wiel, B. J. H., R. J. Ronda, A. F. Moene, H. A. R. de Bruin, and A. A. M. Holtslag, 2002:  
715 Intermittent Turbulence and Oscillations in the Stable Boundary Layer over Land. Part I: A  
716 Bulk Model. *J. Atmos. Sci.*, **59** (5), 942–958, doi:10.1175/1520-0469(2002)059<0942:ITAOIT>  
717 2.0.CO;2.
- 718 van der Linden, S. J. A., and Coauthors, 2019: Large-Eddy Simulations of the Steady Win-  
719 tertime Antarctic Boundary Layer. *Bound.-Layer Meteor.*, **173** (2), 165–192, doi:10.1007/  
720 s10546-019-00461-4.
- 721 van Heerwaarden, C. C., B. J. van Stratum, T. Heus, J. A. Gibbs, E. Fedorovich, and J. P. Mellado,  
722 2017: MicroHH 1.0: a computational fluid dynamics code for direct numerical simulation and  
723 large-eddy simulation of atmospheric boundary layer flows. *Geosc. Mod. Dev.*, **10** (8), 3145–  
724 3165, doi:10.5194/gmd-10-3145-2017.

- 725 Vignon, E., C. Genthon, H. Barral, C. Amory, G. Picard, H. Gallée, G. Casasanta, and S. Argentini,  
726 2017a: Momentum- and Heat-Flux Parametrization at Dome C, Antarctica: A Sensitivity Study.  
727 *Bound.-Layer Meteor.*, **162** (2), 341–367, doi:10.1007/s10546-016-0192-3.
- 728 Vignon, E., F. Hourdin, C. Genthon, B. J. H. van de Wiel, H. Gallée, J.-B. Madeleine, and  
729 J. Beaumet, 2018: Modeling the Dynamics of the Atmospheric Boundary Layer Over the  
730 Antarctic Plateau With a General Circulation Model. *J. Adv. Model Earth Sys.*, **10** (1), 98–125,  
731 doi:10.1002/2017MS001184.
- 732 Vignon, E., and Coauthors, 2017b: Stable boundary-layer regimes at Dome C, Antarctica: obser-  
733 vation and analysis. *Quart. J. Roy. Meteor. Soc.*, **143** (704), 1241–1253, doi:10.1002/qj.2998.
- 734 Zhou, B., and F. K. Chow, 2014: Nested Large-Eddy Simulations of the Intermittently Turbulent  
735 Stable Atmospheric Boundary Layer over Real Terrain. *J. Atmos. Sci.*, **71** (3), 1021–1039, doi:  
736 10.1175/JAS-D-13-0168.1.

737 **LIST OF TABLES**

738 **Table A1.** Overview of the original simulation set-up as used for the VSBL case in van der  
739 Linden et al. (2019). . . . . 37

Table A1. Overview of the original simulation set-up as used for the VSBL case in van der Linden et al. (2019).

Parameter description	Symbol	Value
Grid size	$\Delta$ [m]	0.08
Grid points	$N_x \times N_y \times N_z$	$240 \times 240 \times 240$
Total run time	$t_r$ [h]	23
Cooling time	$t_c$ [h]	6.25
Geostrophic wind speed (VSBL)	$G$ [ $\text{m s}^{-1}$ ]	3.5
Maximum inversion strength	$\Delta\theta$ [K]	25
Subsidence velocity at 100m	$w_s$ [ $\text{m s}^{-1}$ ]	$-4 \times 10^{-3}$
Roughness length for momentum	$z_{0,m}$ [m]	$1 \times 10^{-3}$
Roughness length for heat	$z_{0,h}$ [m]	$1 \times 10^{-4}$
Reference temperature	$\theta_0$ [K]	235
Coriolis parameter	$f_C$ [ $\text{s}^{-1}$ ]	$1.39 \times 10^{-4}$
Acceleration due to gravity	$g$ [ $\text{m s}^{-2}$ ]	9.81
von Kármán constant	$\kappa$	0.4
Smagorinsky constant	$c_s$	0.12
Turbulent Prandtl number	$Pr_t$	1

740  
741  
742  
743  
744  
745  
  
746  
747  
748  
749  
750  
  
751  
752  
753  
754  
  
755  
756  
757  
  
758  
759  
760  
761  
  
762  
763  
764  
765  
766  
  
767  
  
768  
769  
770  
771  
  
772  
773  
  
774  
775  
776

## LIST OF FIGURES

**Fig. 1.** Vertical profiles of (a) the horizontal wind speed components, (b) the potential temperature, (c) the kinematic temperature flux and (d) the contributions to the rate-of-change of potential temperature of the VSBL simulations. Both are averaged over the full horizontal domain and over the final hour of the simulation. Note that, only the lower, dynamically ‘active’ half of the domain is shown. Adapted from van der Linden et al. (2019). . . . . 39

**Fig. 2.** (a) Horizontally-averaged kinematic temperature flux as a function of time and height. (b) The temporal evolution of the kinematic temperature flux at 2.72 m (approximate SBL top in the non-bursting state; purple) and the surface (green). The dash-dotted lines indicate the bursting intervals. Time equal to zero corresponds to the start of the final simulation hour of the original simulation (van der Linden et al. 2019). . . . . 40

**Fig. 3.** Vertical cross sections of the perturbation of the isobaric velocity  $u'$  in the  $xz$ -plane at multiple times during a wave bursting event: (a)  $t = 4800$  s; (b)  $t = 5100$  s; (c)  $t = 5130$  s; (d)  $t = 5160$  s; (e)  $t = 5190$  s; (f)  $t = 5220$  s; and (g)  $t = 5520$  s. Note that only the lower half of the domain is shown. . . . . 41

**Fig. 4.** Normalized power spectrum of (a) the vertical velocity perturbation and (b) the potential temperature. The spectra are averaged over multiple manually selected slices in which wave perturbations are visible. Only part of the wavenumber range is shown. . . . . 42

**Fig. 5.** Normalized vertical profiles at the dominant wavenumber obtained from the simulation (blue) and calculated by the linear stability analysis (red) of (a) the vertical velocity component, (b) the potential temperature, (c) wave momentum flux, and (d) wave temperature flux. Note that, the asterisk indicates the complex conjugate. . . . . 43

**Fig. 6.** Conditionally-averaged profiles during the bursting state of (a) the isobaric momentum flux (solid lines) and the cross-isobaric momentum flux (dash-dotted lines), (b) the kinematic temperature flux, (c) the contributions to the rate-of-change of the isobaric momentum, and (d) the contributions to the rate-of-change of the temperature. Total fluxes are given in black and resolved fluxes in orange. . . . . 44

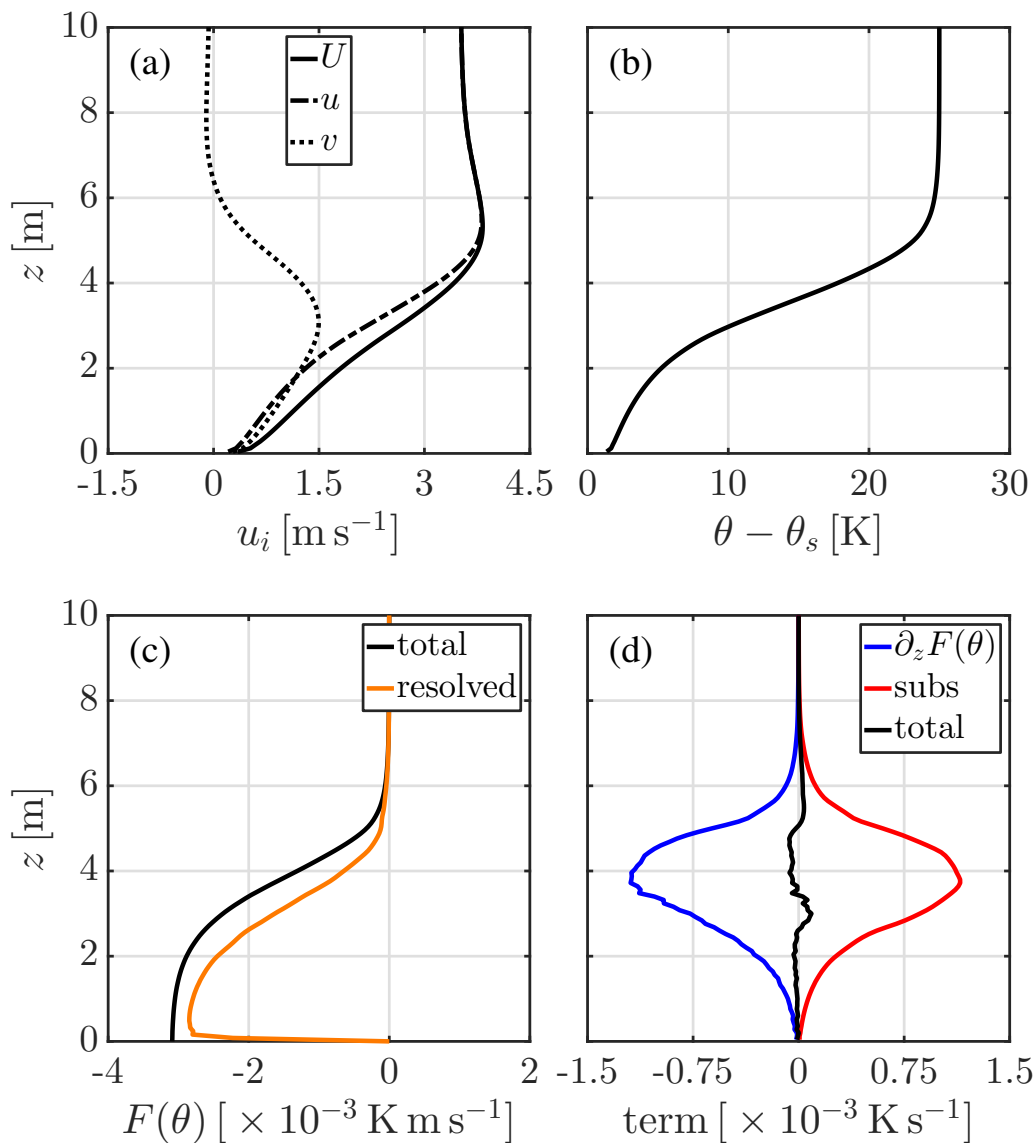
**Fig. 7.** As in Fig. 6, but during the non-bursting state. . . . . 45

**Fig. 8.** Vertical profiles of (a) the total shear squared, (b) the Brunt–Väisälä frequency, and (c) the gradient Richardson number representative for the times  $t = 1400$  (pre-burst), 1600 (after burst, I), 1700 (after burst, II), 1800 (after burst, III), 1900 (after burst, IV) and 2000 s (pre-burst). These are averaged over 20 s. . . . . 46

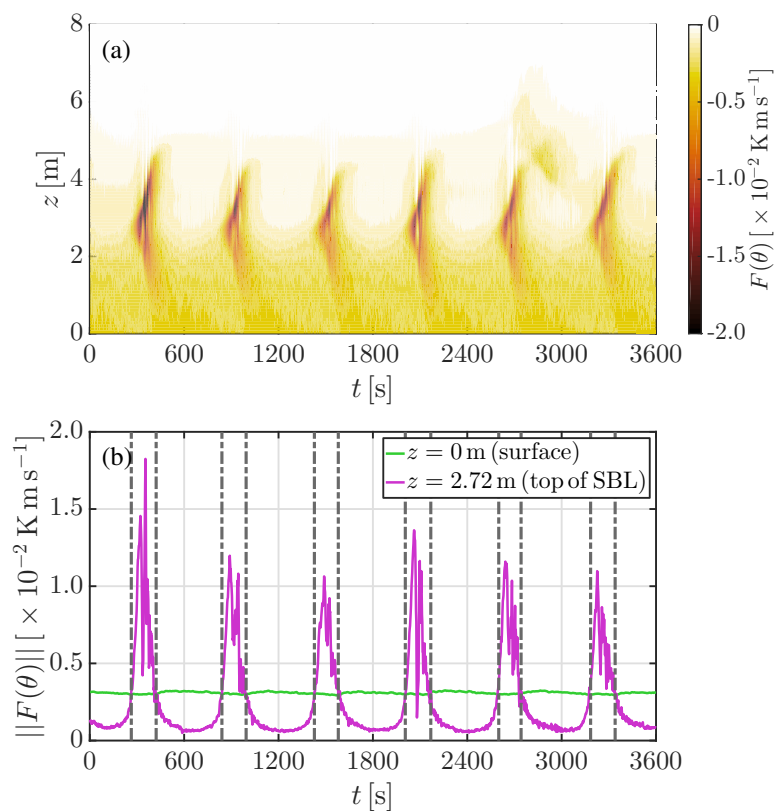
**Fig. 9.** Sketch of changes in the profile of  $u$  centred at the top of the SBL during (a) the non-bursting state, and (b) the bursting state. . . . . 47

**Fig. B1.** Maximum growth rate as a function of the wavenumber for the case considered in the main text. The blue dotted line indicates the wavenumber of the unstable waves in the extended domain simulation. . . . . 48

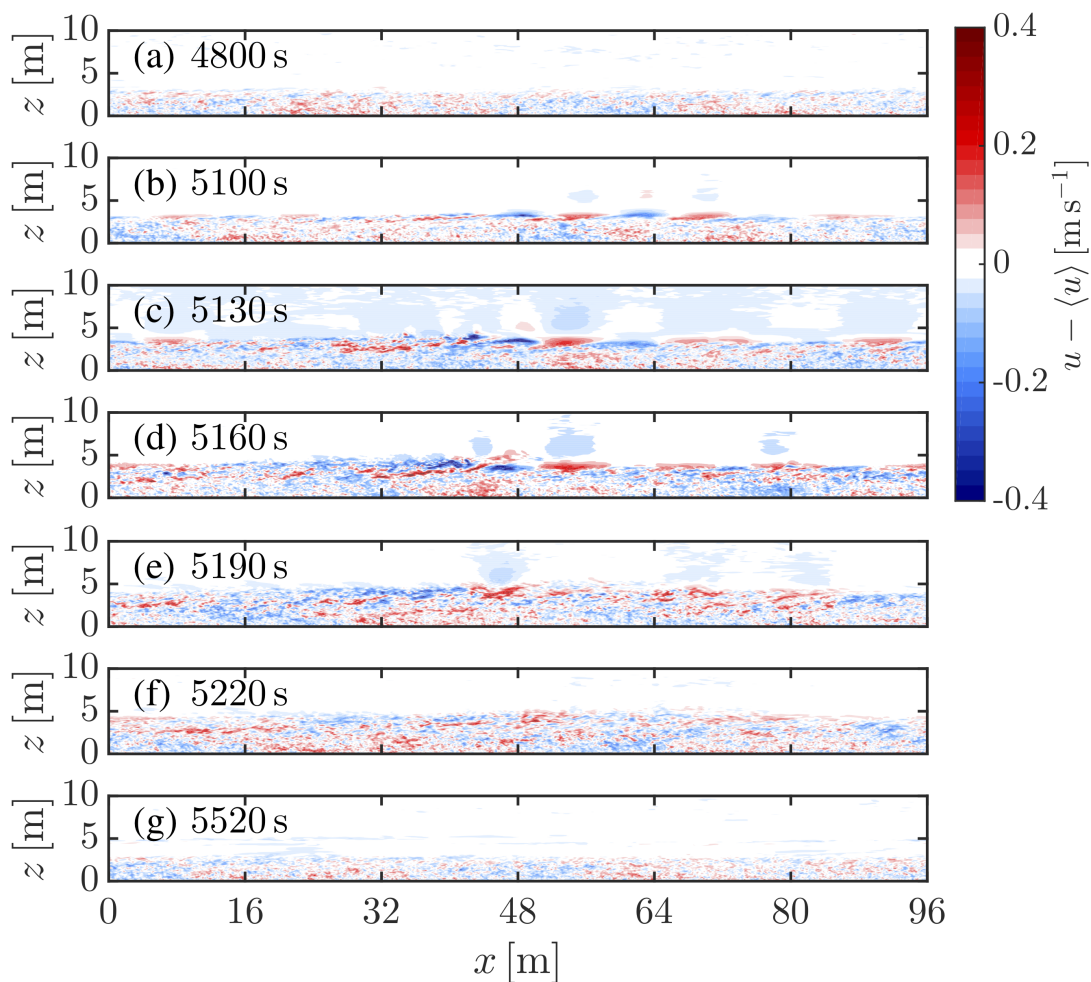
Downloaded from <http://journals.ametsoc.org/jas/article-pdf/doi/10.1175/JAS-D-19-0309.1/4990961/jas-d-190309.pdf> by guest on 26 August 2020



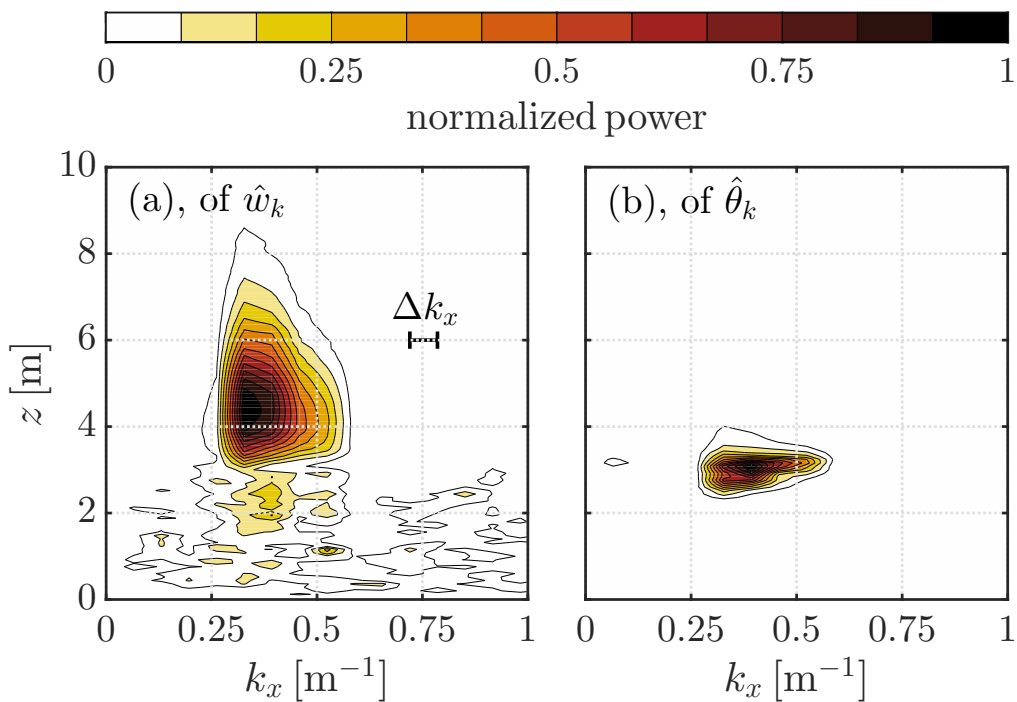
777 FIG. 1. Vertical profiles of (a) the horizontal wind speed components, (b) the potential temperature, (c) the  
 778 kinematic temperature flux and (d) the contributions to the rate-of-change of potential temperature of the VSBL  
 779 simulations. Both are averaged over the full horizontal domain and over the final hour of the simulation. Note  
 780 that, only the lower, dynamically ‘active’ half of the domain is shown. Adapted from van der Linden et al.  
 781 (2019).



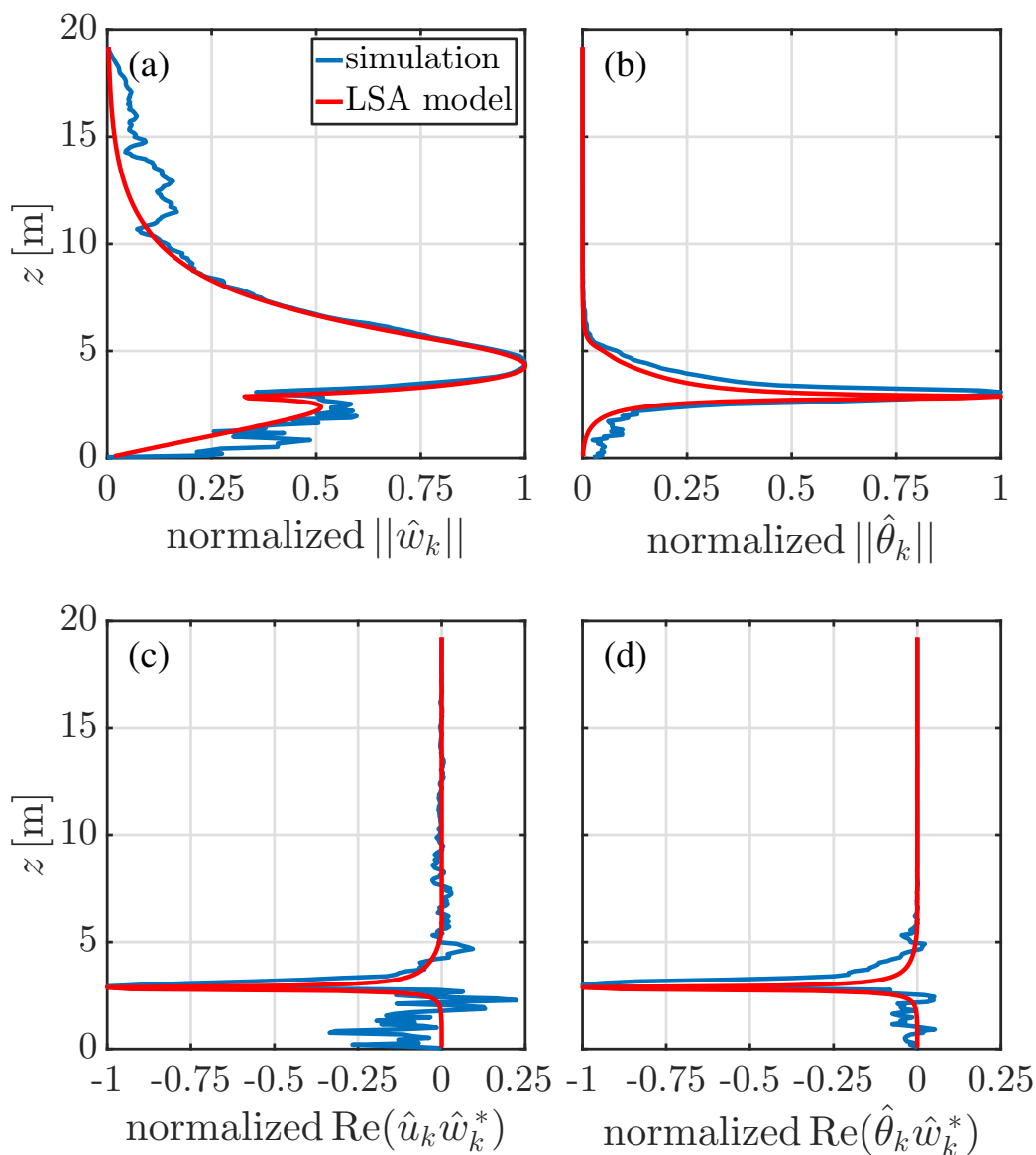
782 FIG. 2. (a) Horizontally-averaged kinematic temperature flux as a function of time and height. (b) The tempo-  
 783 ral evolution of the kinematic temperature flux at 2.72 m (approximate SBL top in the non-bursting state; purple)  
 784 and the surface (green). The dash-dotted lines indicate the bursting intervals. Time equal to zero corresponds to  
 785 the start of the final simulation hour of the original simulation (van der Linden et al. 2019).



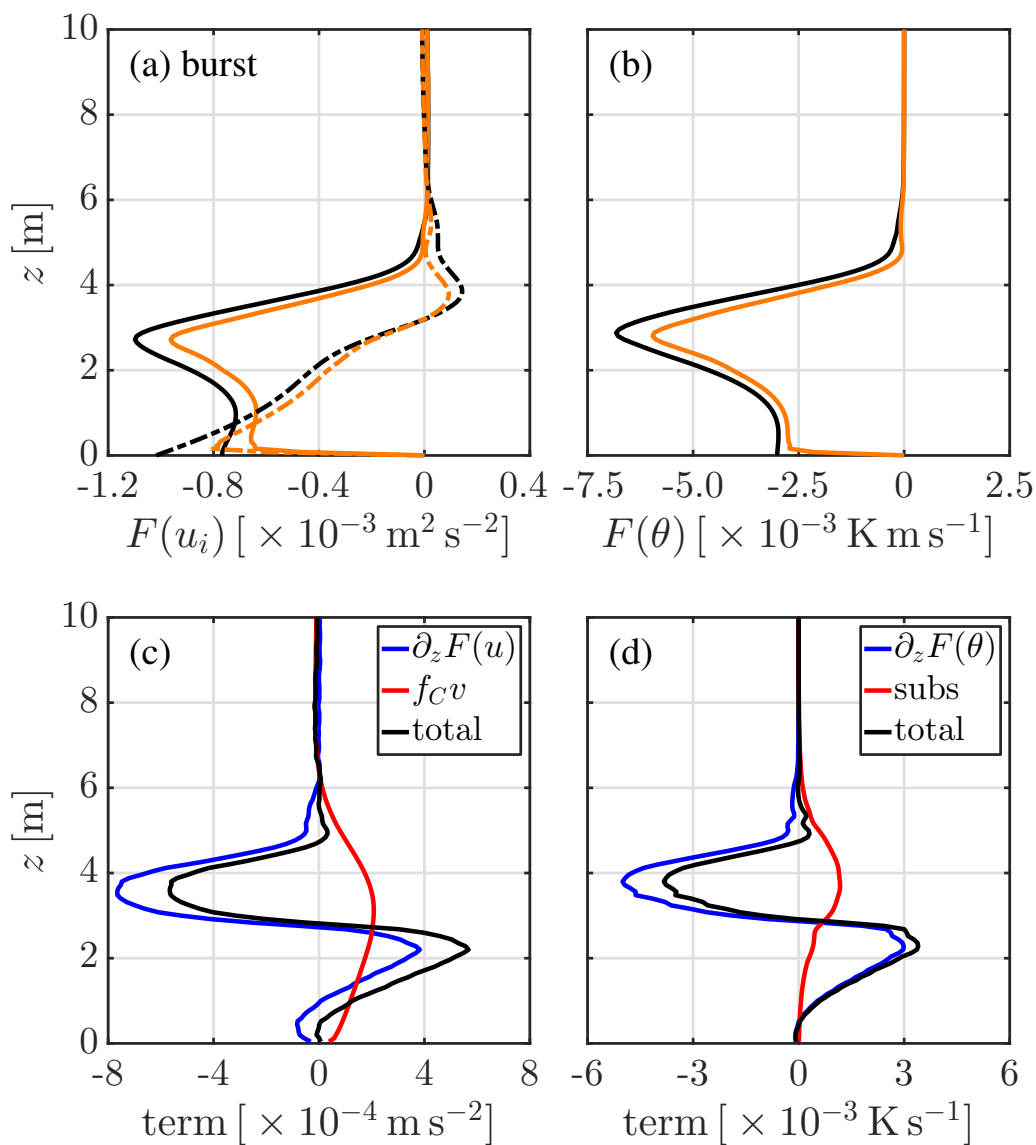
786 FIG. 3. Vertical cross sections of the perturbation of the isobaric velocity  $u'$  in the  $xz$ -plane at multiple times  
 787 during a wave bursting event: (a)  $t = 4800$  s; (b)  $t = 5100$  s; (c)  $t = 5130$  s; (d)  $t = 5160$  s; (e)  $t = 5190$  s; (f)  
 788  $t = 5220$  s; and (g)  $t = 5520$  s. Note that only the lower half of the domain is shown.



789 FIG. 4. Normalized power spectrum of (a) the vertical velocity perturbation and (b) the potential temperature.  
 790 The spectra are averaged over multiple manually selected slices in which wave perturbations are visible. Only  
 791 part of the wavenumber range is shown.



792 FIG. 5. Normalized vertical profiles at the dominant wavenumber obtained from the simulation (blue) and  
 793 calculated by the linear stability analysis (red) of (a) the vertical velocity component, (b) the temper-  
 794 ature, (c) wave momentum flux, and (d) wave temperature flux. Note that, the asterisk indicates the complex  
 795 conjugate.



796 FIG. 6. Conditionally-averaged profiles during the bursting state of (a) the isobaric momentum flux (solid  
 797 lines) and the cross-isobaric momentum flux (dash-dotted lines), (b) the kinematic temperature flux, (c) the  
 798 contributions to the rate-of-change of the isobaric momentum, and (d) the contributions to the rate-of-change of  
 799 the temperature. Total fluxes are given in black and resolved fluxes in orange.

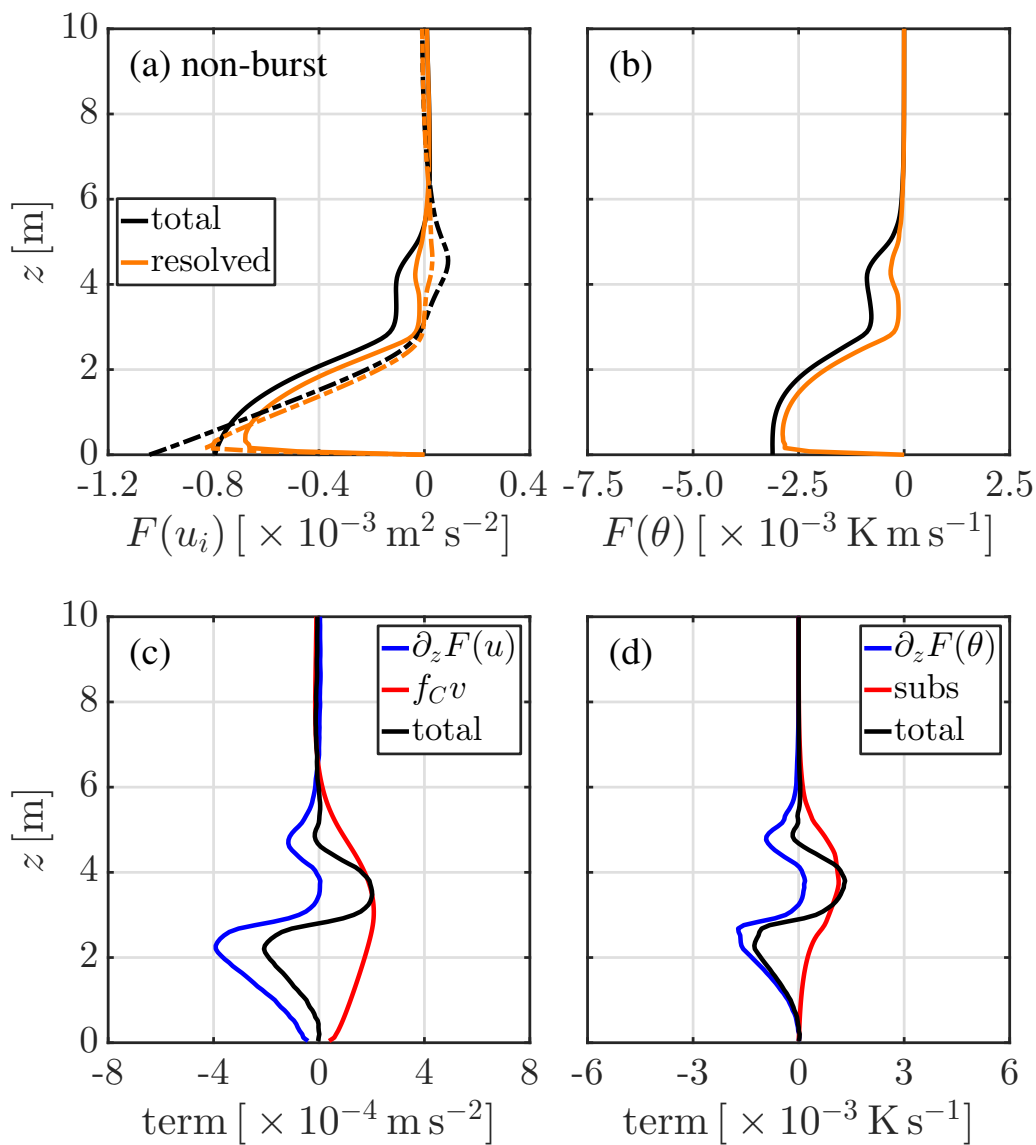
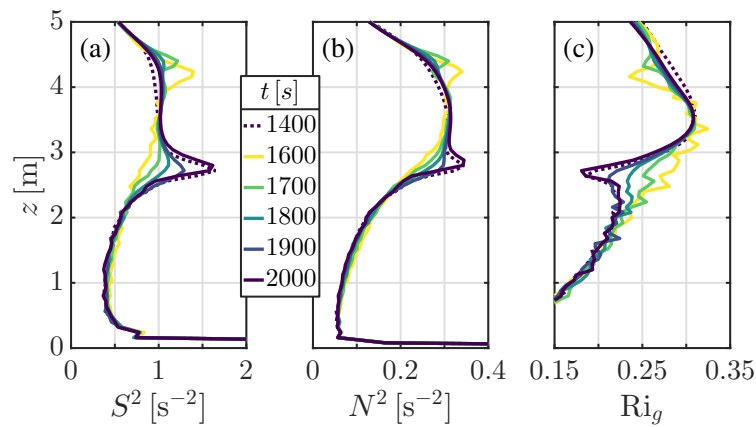
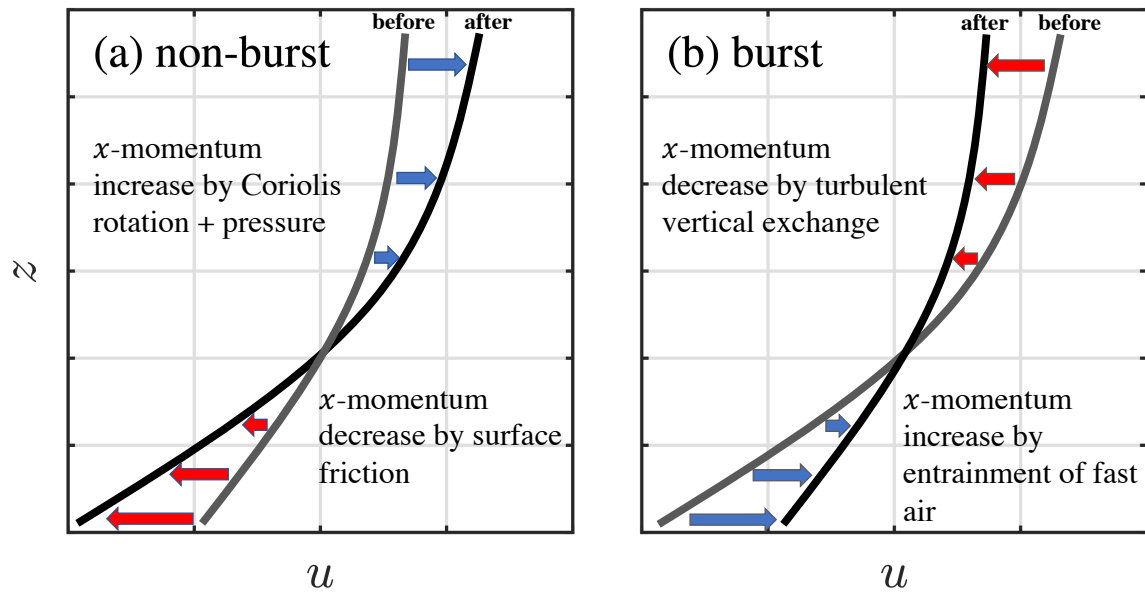


FIG. 7. As in Fig. 6, but during the non-bursting state.



800 FIG. 8. Vertical profiles of (a) the total shear squared, (b) the Brunt–Väisälä frequency, and (c) the gradient  
 801 Richardson number representative for the times  $t = 1400$  (pre-burst), 1600 (after burst, I), 1700 (after burst, II),  
 802 1800 (after burst, III), 1900 (after burst, IV) and 2000 s (pre-burst). These are averaged over 20 s.



803 FIG. 9. Sketch of changes in the profile of  $u$  centred at the top of the SBL during (a) the non-bursting state,  
 804 and (b) the bursting state.

